Synthesis of peptide microstructures for nanogenerators

A DISSERTATION
SUBMITTED TO THE FACULTY OF THE
UNIVERSITY OF MINNESOTA
BY

Vu Nguyen

IN PARTIAL FULFILLMENT OF THE REQUIREMENTS

FOR THE DEGREE OF

DOCTOR OF PHILOSOPHY

Adviser: Dr. Rusen Yang

May 2017

Acknowledgement

First I would like to send my deepest gratitude to my advisor Professor Rusen Yang. Without his continuous support, encouragement, guidance and challenge, I definitely would not be able to finish my research and achieve the results in this thesis. He has not only taught me about new technical knowledge critical to my research, but also about analyzing the key problems, deciding what is important to measure, planning for effective experiments, and presenting the results in a meaningful and interesting way. I still think I have not mastered all what he has taught me yet, and I will need to continue to train myself based on his advice for my future career.

I also wanted to thank my labmates, Dr. Ren Zhu, Wengui Zhang, Kory Jenkins, Dr. Huimin Hao, Alex Jurcoi and Steve Kelly. They have always supported me in everyday life in the lab and are always good friends. I am particularly grateful to Ren and Kory. Ren is my senior labmate and has always been responsive and patient to a lot of my questions, even the silly ones. I also learn great technical and life experiences from Ren. Kory is also super willing to discuss with me about virtually any problem in the lab and, like Ren, share with me a great deal of knowledge I would not have otherwise.

Lastly but never the least, I want to thank my parents for their constant care and encouragement for me throughout my Ph.D. research. Despite half circle of the Earth away, their love for me has always been unconditional and irreplaceable.

Abstract

Electromechanical energy conversion at the small scale utilizing micro/nanomaterials can have significant technological impacts in various areas such as mechanical energy harvesting, tissue engineering, and sensing/actuation. The breakthrough discoveries over the last decade in piezoelectric micro/nanostructures, which converts minute material deformation directly into electrical signal, has spurred intense research in micro/nano scale mechanical energy harvester, also called nanogenerator. Although a variety of advanced inorganic piezoelectric micro/nanostructures have been fabricated, little progress has been made for bioinspired piezoelectric materials, which can enable biocompatible and biodegradable energy harvesting.

Meanwhile, piezoelectricity has been widely observed in biological materials such as bone, collagen, viruses and other protein-based materials. Diphenylalanine (FF) peptide, which consists of two naturally occurring phenylalanine amino acids, has attracted significant research interest due to its exceptional mechanical and piezoelectric properties as well as rich biological properties. Thus FF is promising to become one of the most technologically important bioinspired materials for piezoelectric devices, such as mechanical energy harvester. However, many challenges exist in realizing the potential of piezoelectric FF peptide, such as the lack of scalable structural alignment, lack of controllability of polarizations and lack of prototyped device. This thesis aims to address those challenges to advance the applications of FF peptide towards piezoelectric nanogenerator (PENG) and beyond.

As an alternative to PENG, which converts minute material deformation into electricity, triboelectric nanogenerator (TENG) has also been proposed recently to harvest energy from large motion through a combination of triboelectric effect and electrostatic induction. Since tiny material deformation and large motion are usually available together, advances in nanogenerator are needed to harvest them effectively. Due to the apparent complementary energy conversion mechanisms of piezoelectric and triboelectric effects, performance of TENG in various environmental conditions will be studied, and hybridization of PENG and TENG into one device will also be explored as an approach to enhance the outputs of the mechanical energy harvester.

In overview, first this thesis will develop a novel low-temperature epitaxial growth process to address the challenge of synthesizing aligned piezoelectric FF peptide structures in a scalable and controllable manner. Second, the random orientation and unswitchability of its polarization will be addressed by modifying the growth parameters and including an applied external electric field during the growth. The improved FF microstructures will be used to demonstrate the first peptide PENG. Third, a standalone TENG will be studied for its operation in various environmental conditions, verifying its wide applicability. Finally, a hybrid nanogenerator structure will be proposed to constructively combine the outputs of FF peptide PENG with a TENG, and the hybrid energy conversion process will be experimentally verified.

Table of Contents

List of Tables

List of Figures

CHAPTER 1. INTRODUCTION

1.1. Technological significance of small-scale electromechanical energy conversion

Mechanical energy is an abundant and renewable energy source in our environment, which exists in various forms such as human movement, material deformation, engine vibration, wind, water flow, ocean wave, etc. While exploiting them at large scale has become reality through hydroelectric dams and wind turbine farms for grid-scale power source, energy conversion at small scale had not seen many significant advances until 2000s. However, recent technological advances and scientific discoveries suggest that innovation of the material for electromechanical conversion at small scale can indeed be an enabling factor. The areas that will potentially be impacted most by such innovations are (1) mechanical energy harvesting, (2) tissue engineering and (3) sensing and actuation.

(1) Mechanical energy harvesting

With the development of the internet and the internet of things (IoT), the number of independent sensor nodes increases significantly to collect large amount of data for advanced applications in areas such as health, structural and environmental monitoring. As the sensor network expands, replacing each individual battery for each node can become costly or even impractical. For example, if sensors are to be mounted on each individual blade in a large wind turbine farm for structural health monitoring, using battery or wired power would present a significant design and maintenance problem. Another example is implanted medical devices for patient health monitoring. Using the battery or wiring to an

external power source may require surgery for maintenance and reduce quality of patient care. In those cases, mechanical energy is available in the surrounding, and the ability to harvest it effectively can enable independent sensor nodes. A scheme for such self-powered system, shown in Figure 1, was proposed by Professor Zhong Lin Wang, which includes a nanogenerator as a power source, a capacitor as energy storage, sensor, and transmitter [1]. Materials with efficient electromechanical energy conversion for the nanogenerator to improve the electrical outputs, which will be discussed later in this chapter, can expand the applications of the self-power system.

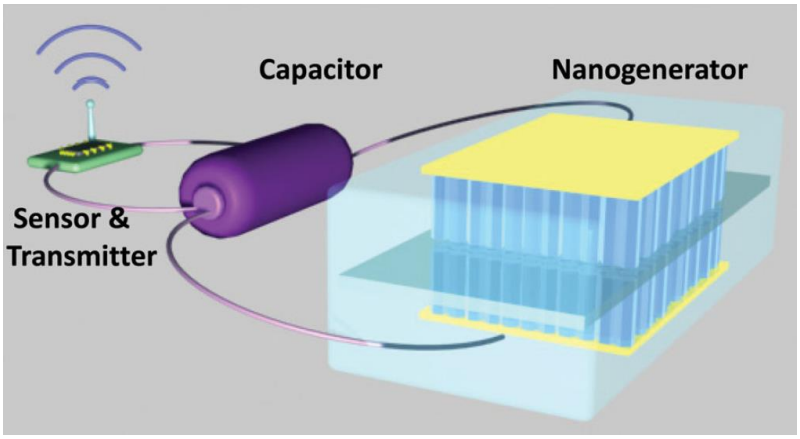

Figure 1. Schematic of a self-powered system powered by a nanogenerator [1].

(2) Tissue engineering

Besides energy application, electrical signal produced by mechanical stimulus may also be used in manipulating living organisms. It is well-known that piezoelectric effect exists in human bone [2, 3], and the electric potential produced by the stress on bone plays an important role in bone growth [4, 5]. At cellular level, extracellular electric field has also been demonstrated to significantly affect not only cell growth, but also cell division

and migration [6-8]. Figure 2 shows the effect of electric field on neurite cells and corneal epithelial cells.

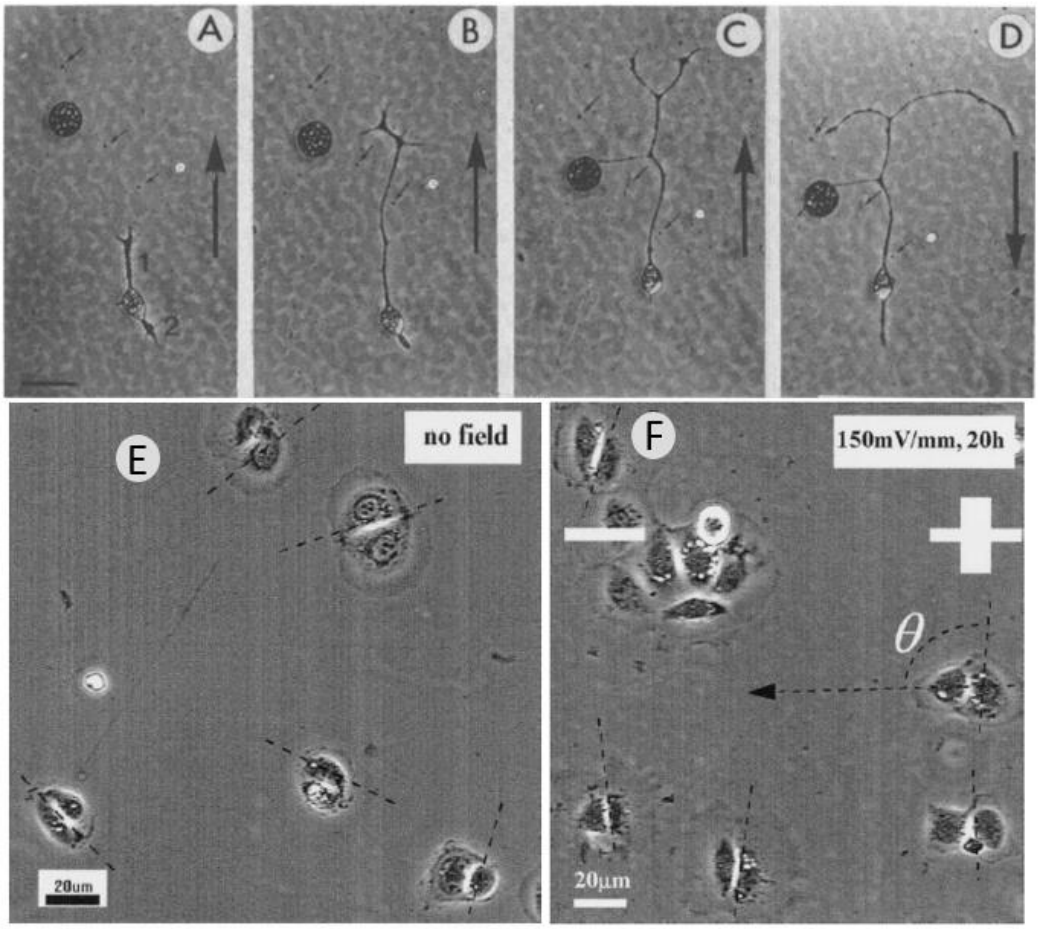

Figure 2. Effect of electric field on biological activities. On neurite cell growth (a-d) and corneal epithelial cells division (e-f). Direction of electric field is shown by the arrows (a-d) and the polarity (f). No electric field is applied in (e) [6, 7].

The opportunity to manipulate biological activities at the cellular level has spurred further research to explore the use of piezoelectric materials, which can directly convert mechanical stimulus into electrical signal, for tissue engineering to promote the desired

cell growth. The use of piezoelectric material can eliminate the need of implanted wire leads and external power source, which can have meaningful impact in wound healing and regenerative medicine [9]. Poly(vinylidene) fluoride (PVDF) has been the most widely tested piezoelectric substrate for cell culturing. Data have shown that poled PVDF significantly promotes cell growth *in vitro* for both rat and human cells, while unpoled PVDF does not [10-12]. Although static condition still improves cell growth and differentiation thanks to the charges produced by the inherent polarization in piezoelectric materials, dynamic condition, induced by mechanical shaker or ultrasound, was found to further enhance the result [5, 12].

Despite the promising early studies, the overwhelming use of PVDF and other inorganic piezoelectric materials presents a bottleneck in biodegradability and biocompatibility. Since piezoelectric effect is widely observed in the biological world itself [2, 13, 14], engineered bioinspired piezoelectric material can be a potential material platform for future tissue engineering application.

(3) Sensing and actuation

Electromechanical resonators have been widely researched for various applications in telecommunications, automobiles [15-17] and biosensing [18-20]. In biosensing, resonators offer advantages over other mechanisms, such as electrochemical, optical and calorimetric, thanks to their high sensitivity and small form factors. The two common types of biosensing resonators are surface acoustic wave (SAW) resonators and bulk acoustic resonators (BAR). Most of them consist of a piezoelectric thin film, which produces

resonating waves when an alternating voltage is applied across the electrodes. The typical structures of the resonators are shown in Figure 3. When a species is attached to the functionalized surface, the resonance frequency is shifted an amount corresponding to the amount of the attached species. The sensitivity is determined by not only the mechanical and piezoelectric properties of the film, but also by its ability to be functionalized to attach to the species it needs to detect. Therefore, the choice of the piezoelectric material can determine the scope of application for the sensor.

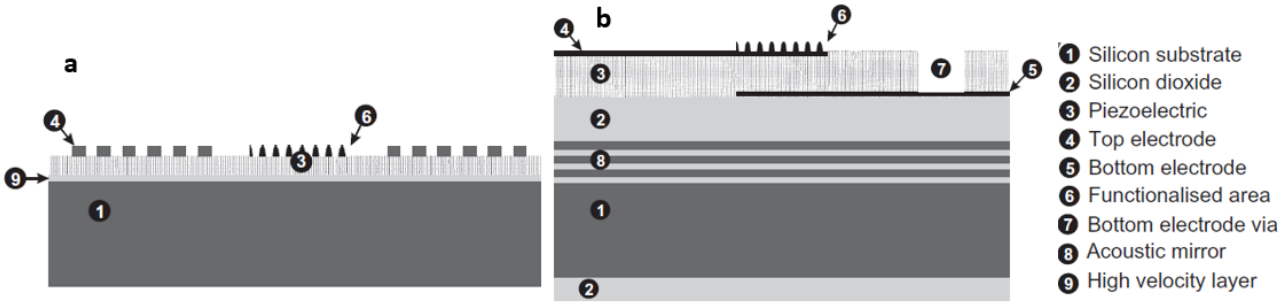

Figure 3. Structures of acoustic resonators for biosensing. Surface acoustic wave (SAW) resonator (a) and film bulk acoustic resonator (FBAR) (b) [18].

1.2. Nanogenerators

The application of focus of this thesis will be mechanical energy harvester. The small energy harvesters with micro/nanomaterials and structures are nowadays called nanogenerators. The development of the nanomaterials and nanotechnology leads to the first demonstration of the nanogenerator in 2006 with zinc oxide (ZnO) nanowires [21]. Using micro/nanomaterials provides many advantages over their bulk counterparts, including reducing the reliance on complex and expensive top-down cleanroom processes, higher crystallinity with less defects, and higher surface-to-volume ratio, etc. Since then

various nanogenerators have been developed using piezoelectric [22-24], triboelectric [25-27], pyroelectric [28, 29], and thermoelectric effects [30, 31]. This thesis will focus on mechanical energy harvesters, i.e. piezoelectric nanogenerators (PENG) and triboelectric nanogenerators (TENG), with an emphasis on bioinspired PENG.

Figure 4 shows a basic PENG unit which consists of a single lateral piezoelectric ZnO nanowire [32]. A strategy to scale up this PENG unit is fabricating an array of many aligned nanowires and connecting them either in series or parallel [22, 33, 34]. Thus the ability to align the structures in a scalable manner is key to enhance the electromechanical energy conversion in the PENG.

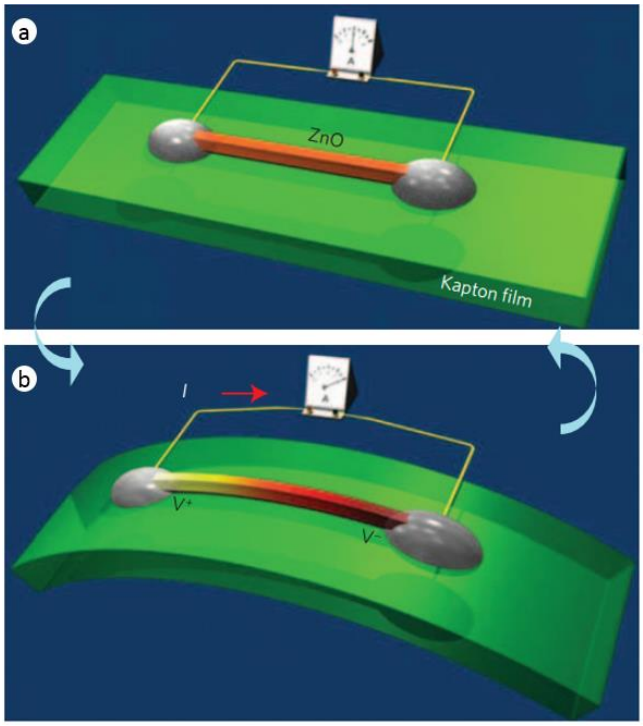

Figure 4. ZnO nanowire on a flexible substrate as a nanogenerator. There is no current flow to the external circuit with an unstretched nanowire (a). The bent substrate induces a tensile stress in the piezoelectric nanowire and a voltage is produced, resulting in current flow (b) [32].

In 2012 triboelectric nanogenerator (TENG) was first proposed as another promising technology to also convert mechanical energy to electricity [25]. TENG is based on the triboelectrification and electrostatic induction. In triboelectrification, when two materials come into contact, one of them will charge positively and the other will charge negatively. The charge affinity of each material can be ranked in an empirical table called triboelectric series, shown in Figure 5, for which many versions exist [27, 35]. Despite serving as a guideline, the series is not sufficient to predict all the charging behaviors of

the contacting materials, due to the influence of many other factors such as the surface cleanliness, or surrounding conditions.

Figure 5. A triboelectric series [27].

TENG has been demonstrated in four modes of operation, shown in Figure 6, namely vertical contact-separation mode, contact-sliding mode, single-electrode mode and freestanding triboelectric-layer mode [26]. While PENG captures the mechanical energy from the minute deformation of materials, TENG harvests the energy from large motion. Thus TENG can work in complement with PENG to effectively harvest more of the

available mechanical energy. This thesis will explore the integration of TENG with PENG for enhanced outputs.

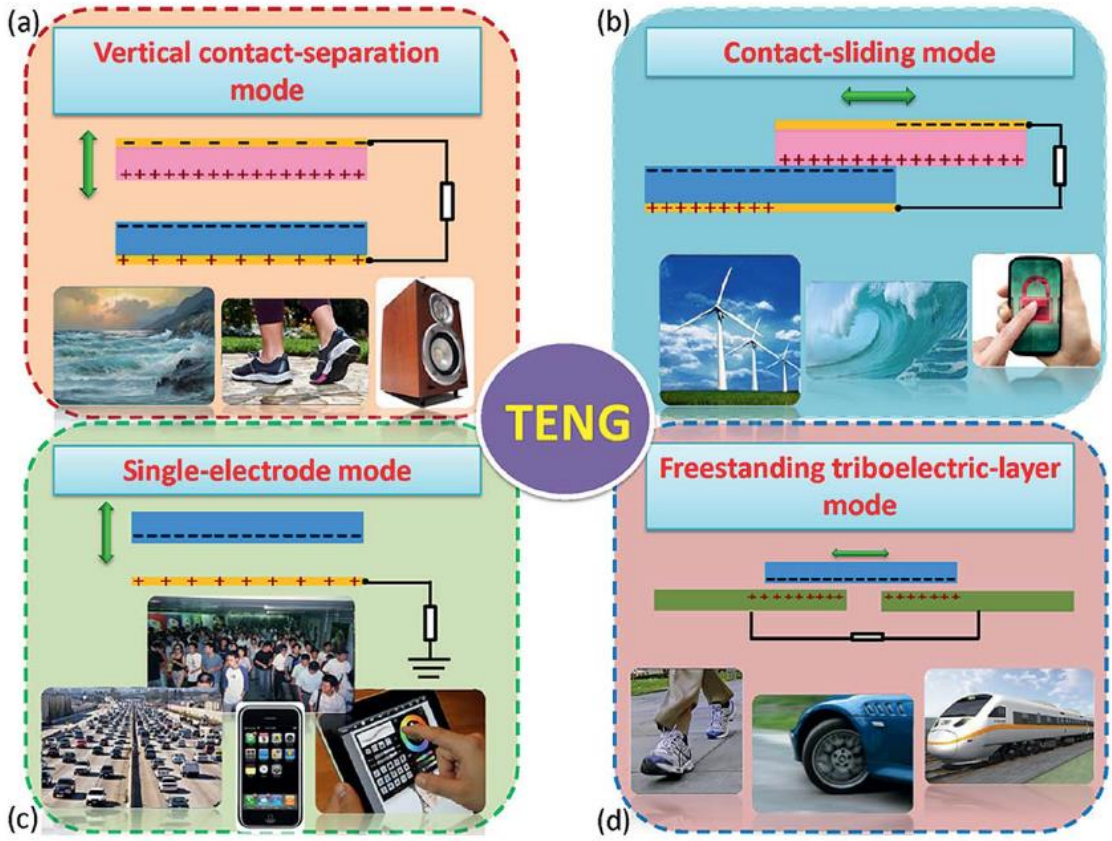

Figure 6. Four operation modes of TENG [26].

1.3. The emerging piezoelectric diphenylalanine (FF) peptide

1.3.1. Nanostructures of traditional piezoelectric materials

Piezoelectric materials have found numerous applications in modern electromechanical devices in various industries such as medical instruments, telecommunications, and automobiles. Recently, there has been an increasing interest in fabricating micro/nanostructures of piezoelectric materials, such as semiconducting oxides

nanowires/belts/helixes [36-38], PZT nanoribbons [39, 40], BaTiO3 nanowires [41], PVDF nanowires [42]. Figure 7 shows ZnO nanowires array whose orientation can be controlled in vertical, horizontal and diagonal directions [38].

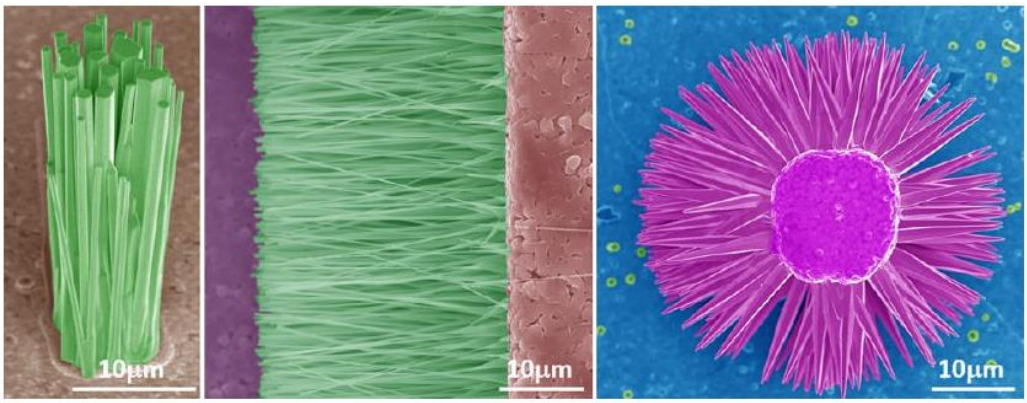

Figure 7. ZnO nanowire array with orientation control [38].

The fabrication techniques can also achieve designs that can interface with biological systems, such as PZT nanoribbons for cellular deformation monitoring [40]. Figure 8 shows the SEM images of such interface.

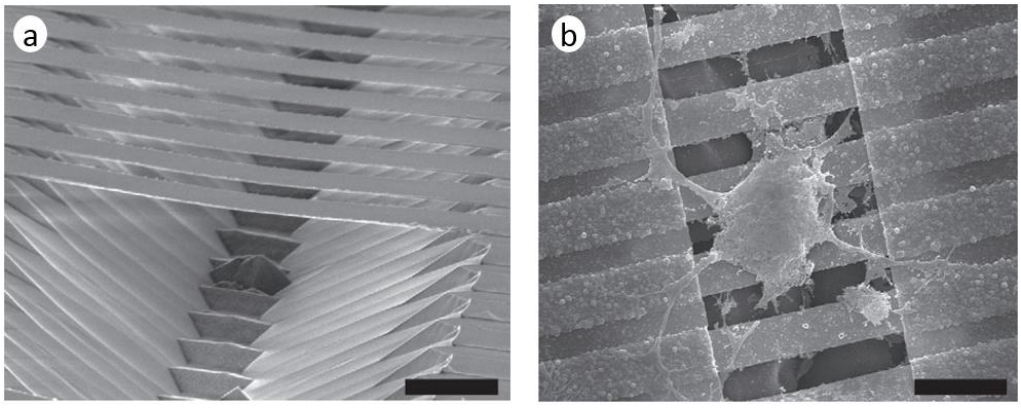

Figure 8. PZT nanoribbons interfacing with cell. Suspended PZT nanoribbon, scale bar is 5µm (a), and a single PC12 cell directly interfaced with PZT nanoribbons, scale bar 15µm (b) [40].

Although many advanced piezoelectric micro/nanostructures have been developed and their potential for use with biological systems has been demonstrated, most of them are non-biodegradable and non-biocompatible. Besides quartz and polyvinylidene fluoride (PVDF), a vast majority of them are heavy-metal-based inorganics which can be toxic to living organisms due to the dissolution of ions such as Pb^{2+} and Ba^{2+}. The most widely studied organic PVDF is not biodegradable and hard to be functionalized due to the lack of biologically functional groups in its molecules.

1.3.2. Piezoelectric FF peptide

Piezoelectric phenomena have been widely observed in natural materials like bones [2, 3], collagen [13, 14], virus [43, 44], and a variety of protein-based materials [45]. Peptide is a class of materials whose molecule consists of a short chain of amino acids connected together through peptide bonds, similar to protein but with fewer number of amino acids. There has been a significant research interest in the synthesis of peptide self-assembled nanostructures, most commonly nanotubes, thanks to their rich biological properties, the wide choices of the amino acid building blocks, and various self-assembly mechanisms [46-49]. Among them, diphenylalanine (FF) peptide, whose molecule is composed of the naturally occurring amino acid phenylalanine (technically abbreviated as letter "F"), is one of the most widely studied thanks to its exceptional piezoelectric properties [50], remarkable mechanical properties [51, 52], and high biocompatibility with low to no cytotoxicity [53-55]. FF nanotube was first observed while being studied as a recognition motif of the amyloid fibrils in Alzheimer disease [49]. Further studies into FF crystal structures reveals a hexagonal symmetry in which six FF molecules are linearly

connected through hydrogen bond in a spiral manner into a unit cell, which is shown in Figure 9a-b. Translation of this unit cell in the longitudinal direction forms a nanochannel, shown in Figure 9c, and stacking the nanochannels side by side through π-π interactions scales up FF crystal, shown in Figure 9d [56, 57]. The available NH_3^+, $COOH^-$ and the two phenylalanine residues at the outer surfaces of the crystal provide active sites for chemical functionalization.

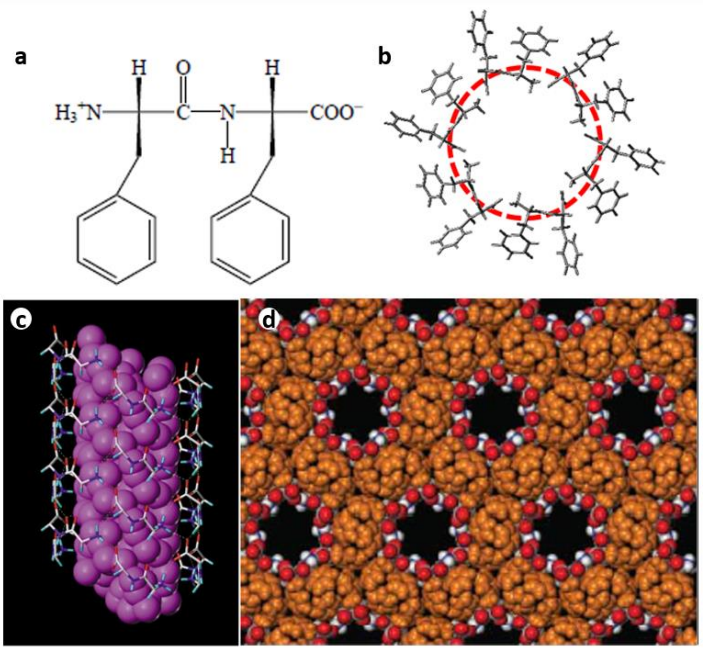

Figure 9. Model of FF molecule and crystal. FF molecule in a zwitterion form (a), a unit cell in FF crystal (b), model of a FF nanochannel filled with water molecules (c), and FF hexagonal crystal structures (d) [56, 57].

Due to the non-centrosymmetry which lacks an inversion center, FF crystal exhibits a strong piezoelectricity. Early effort to measure the piezoelectricity in FF nanotubes using Piezoresponse Force Microscopy (PFM), shown in Figure 10, demonstrated a very strong

shear piezoelectric coefficient $d_{15} \approx 60$ pm/V, which is comparable to the classical piezoelectric lithium niobate [50]. The study also confirms that the polarization of FF nanotube is along the tube axis with no radial component.

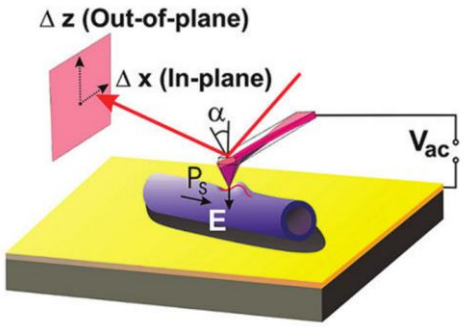

Figure 10. Measurement of shear piezoelectricity in FF nanotube using PFM. The polarization Ps is shown to orient only along the tube axis [50].

This polarization results from the head-to-tail ordering of FF molecular dipoles, each of which points from the carboxylic end to the amino end [56, 58, 59]. These dipoles are bonded in a helical manner, so the resultant total dipole points along the axis of the helix, which is the c-axis of the crystal. This total dipole is verified by the alignment of freestanding tubes along the external electric field as shown in Figure 11a-b [58]. The dipole orientation also causes the two end surfaces of the FF micro/nanotubes to exhibit either positive or negative charge, Figure 11c [58].

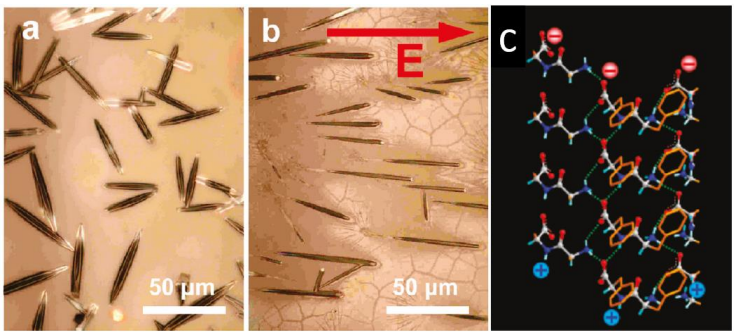

Figure 11. Effect of external electric field on the orientation of freestanding FF microtubes. (a) Orientation without E, (b) orientation with E, and (c) model of the charges at the two ends of the FF nanochannel [58].

Although single FF nanotube has strong piezoelectricity, adjacent nanotubes were shown to exhibit polarization in opposite directions [50], and further studies also point out that this polarization is unswitchable by an applied electric field [60]. Therefore, despite strong piezoelectricity and inherent biocompatibility as well as biodegradability, the cancellation of the adjacent polarizations in an FF array, as well as the lack of macro-scale aligned structures, present a bottleneck in realizing scalable applications of FF-based material.

1.3. Scope of this thesis

While the far-reaching goal is to realize biodegradable and biocompatible piezoelectric solutions for various energy, biomedical applications and beyond, this thesis will focus on the nanogenerator application of piezoelectric FF peptide, and the challenges to improve its outputs. The challenges that will be addressed in this thesis are as follow.

(1) Macro scale structural alignment [61]

Currently there is a lack of controllable and scalable low-temperature synthesis method to produce aligned piezoelectric FF arrays. Chapter 2 demonstrates a novel low-temperature epitaxial growth process that produces a vertically aligned microrod array. Details of the obtained structures, effects of process parameters and material characterization are also discussed.

(2) Control of polarization and demonstration of a FF peptide PENG [62]

The unswitchability of the polarization in FF crystals hinders the realization of macro scale piezoelectricity, which would require all electrical dipoles in the crystal to point in the same direction. Chapter 3 discusses the effect of applied electric field during the epitaxial growth to obtain uniform polarization in opposite directions. The epitaxial growth is modified to occur at a slightly elevated temperature to obtain microrod arrays with better uniformity and piezoelectricity. To demonstrate the usefulness of the obtained arrays, FF peptide PENGs are fabricated and their performances are characterized.

(3) Integration with triboelectric nanogenerator [63][106]

The complementary energy conversion processes of PENG and TENG prompts at a hybrid device. To realize this approach, Chapter 4 develops a new TENG and characterizes its performance in various environmental conditions. Then Chapter 5 proposes an architecture to integrate FF peptide PENG with TENG to produce complementary outputs.

CHAPTER 2. ROOM-TEMPERATURE EPITAXIAL GROWTH OF ALIGNED FF PEPTIDE MICROSTRUCTURES

2.1. Previous growth techniques

Many techniques have been developed in the last decade to obtain aligned FF micro/nanostructures, and a large number of studies have been focused on high-temperature-based processes [64-69]. Figure 12 described a vapor deposition process proposed by Adler-Abramovich *et. al.* which can produce vertically aligned nanowire/nanotube array.

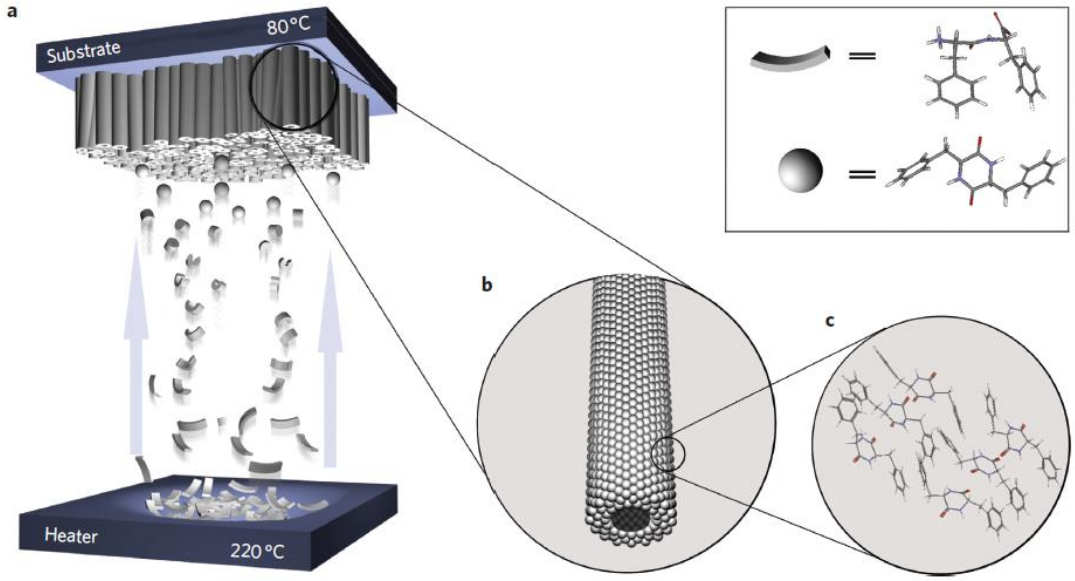

Figure 12. High-temperature vapor phase growth of FF nanotubes array. As the FF powder evaporates, linear FF is transformed into cyclic FF [64].

Although the high temperature processes like vapor deposition can produce crystalline aligned structures on centimeter-scale or larger substrates, it causes peptide materials to undergo an irreversible phase transformation due to the cyclization of the amino acid chain [64, 70]. For FF peptide, this phase transformation was found to occur at around 150^{o}C, as revealed by Differential Scanning Calorimetry (DSC) and X-ray Diffraction (XRD) data in Figure 13. Therefore, processes using temperature higher than the phase transformation temperature can deprive the FF peptide materials of some interesting properties, such as piezoelectricity, which is associated with the linear FF molecules [60].

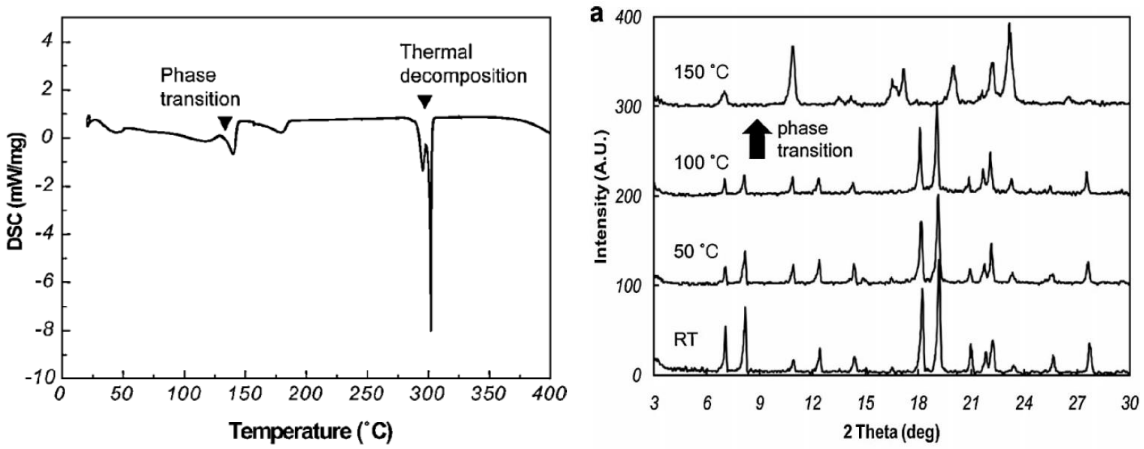

Figure 13. Temperature-induced phase transition of FF crystalline structures [70].

The irreversible phase change prompt many studies to keep the growth process at room-temperature, and the solution-based approach has been widely employed [58, 71-74] thanks to a variety of available solvents for FF [75]. This approach involves inducing FF self-assembly in the solvents by various means such as drying [38, 58, 71, 76] supersaturation [77, 78] or agitation [79]. Figure 14 describes a simple solution-based

drying process that can produce bundles of vertical nanotubes. However, although the available methods can synthesize diverse structures of FF, the array sizes are small, in millimeter or micrometer scale, which hinders fabrication of useful devices.

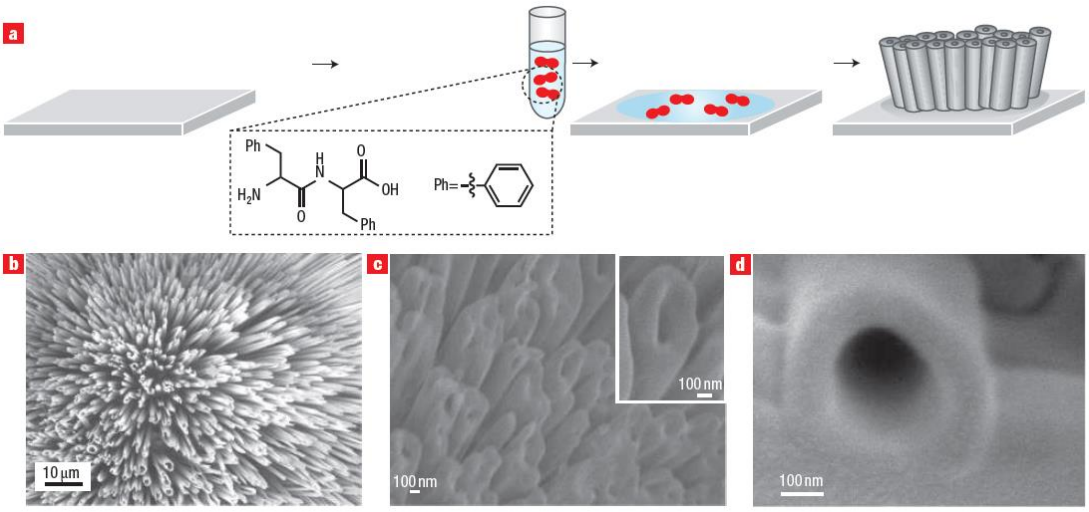

Figure 14. A typical room-temperature solution-based growth of FF nanostructures [71].

This chapter will describe a novel low-temperature growth approach to produce arrays of FF peptide towards fabricating useful FF-based device.

2.2. Room-temperature epitaxial growth process

Diphenylalanine lyophilized powder H-Phe-Phe-OH (FF) was purchased from Bachem and stored in an enclosed dry container at 0^{o}C. 1,1,1,3,3,3-hexafluoro-2-propanol (HFP) was purchased from Sigma Aldrich and stored in a dry container under ambient conditions. An overview of the fabrication process is shown in Figure 15a-c. The process started with casting an amorphous layer as shown in Figure 15a. First, the FF stock solution was prepared by dissolving lyophilized FF powder in HFP to a concentration of 50mg/mL

in a glove box (water content <1000ppm) to minimize water absorption to the source materials. 25μL of the stock solution was then dropped on an ITO-coated silicon substrate placed in a desiccator. The drop was quickly vaporized as the desiccator was pumped down to 200 Torr in 10 seconds and then vented with compressed dry air (water content <6ppm). A transparent amorphous film was formed on the substrate after the evaporation completed. The low water vapor content in the growth environment with relative humidity (RH) lower than 50% is essential to prevent unintentional crystallization of the amorphous film [69].

This amorphous film was then transferred to an enclosed box which was connected in a closed loop of flowing moist air with RH~100% (Figure 15b). The amorphous film was intentionally crystallized into a seed layer by vigorously circulating the humid air through the enclosed box for 90 seconds. The epitaxial growth from the seed layer was achieved by the precipitation of a saturated FF aqueous solution (Figure 15c). First a concentrated FF aqueous solution was prepared by mixing 75mg FF with 50mL deionized (DI) water and kept in an oven at 65^{o}C until the FF powder was fully dissolved. The substrate with the prepared seed layer was placed floating upside down on the surface of concentrated FF solution right after the solution was taken from the oven to the ambient condition. Ventilation from a small fan was used to facilitate the cooling to room-temperature and the evaporation of water in the concentrated FF solution. Most of the water had evaporated after about 6 hours. The substrate with FF peptide microrods was then taken out, briefly cleaned with DI water, and dried with compressed air.

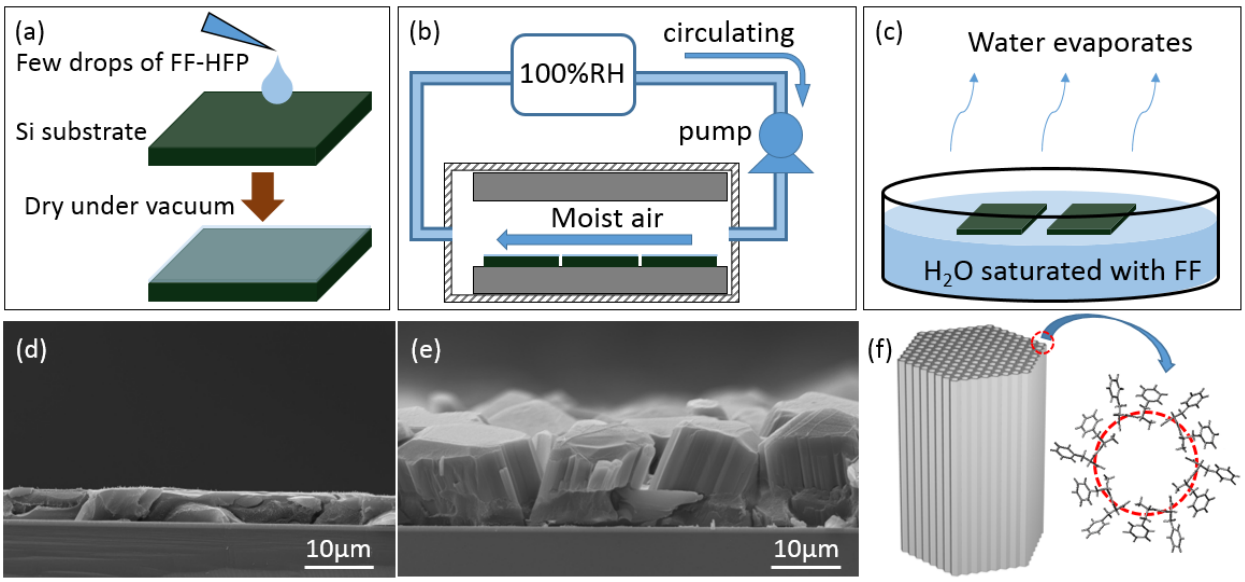

Figure 15. FF microstructures fabrication process. Schematic illustration of the process (a-c) and SEM image and model of FF peptide microrods (d-f). (a) Formation of an amorphous FF peptide layer on the substrate. (b) Formation of the FF peptide seed layer through the crystallization of the amorphous layer from (a). (c) Self-assembly of FF peptide molecules for epitaxial growth of FF peptide microrods. (d) Side SEM image of the seed layer from (b). (e) Side SEM image as-grown FF peptide microrods from (c). (f) Illustration of FF peptide microrods with hexagonally arranged nanochannels. The enlarged circle illustrates a nanochannel enclosed by six FF peptide molecules.

The synthesized samples were coated with either gold or platinum and analyzed using a field emission JOEL 6500 scanning electron microscope (SEM). Figure 15d and e show the cross section of the crystalline seed layer and FF microrods after 6 hour room-temperature epitaxial growth. Their height is approximately 10μm from the seed layer, or 15μm from the substrate. The microrods were solid with the diameter mostly ranging from 10μm to 20μm, which forms the largest reported solid microrod array to our best

knowledge [79]. The growth of the microrods is the result of the self-assembly of FF molecules on the seed layer as the saturated FF aqueous solution evaporates. As shown in Figure 15f, the FF peptide microrod can be considered as a bundle of idealized close-packing of hydrophobic nanotubes with hydrophilic hollow channels. The channel is of a van der Waals' diameter of ~10 Å and filled with water molecules [56]. Six FF peptide molecules constitute the circumference and the translation of those molecules along the axial direction creates each tube. The side chains with neutral phenyl group emanate from the channel cores and are exposed from the side wall. The more active carboxyl group and amine group forms a hydrogen bond and connects the FF peptide molecules along the axial direction. Thus, unlike the neutral phenyl groups on the wall, the positively charged amine groups or negatively charged carboxyl groups at the end of the nanochannel assist the self-assembly of FF peptide molecules for the fast growth along axial direction. Consequently, a highly textured seed layer with nanochannels preferentially orientated normal to the substrate is critical for the epitaxial growth of high quality FF peptide nano or microstructures with desired alignment.

The SEM images in Figure 16a and b show a vertical area in the seed layer, which is approximately a hexagon, suggesting a hexagonal crystal structure as shown in Figure 15f and Figure 9. The zoom-in image in Figure 16b confirms this vertical seed is solid, and the scattered nanowires imply that the top surface has active sites for the self-assemble of FF molecules. The vertical seed particles are expected to initiate epitaxial growth of FF peptide crystals. An FF peptide microrod grown from the seed layer in Figure 15d is shown in Figure 16c, along with the top view of the micro rod tip in Figure 16d and the side wall

with vertical strips in Figure 16e. The rough tip and smooth side wall of the micro rod is a result of the fast growth along the axial direction and consistent with the observation that there is no branch formed.

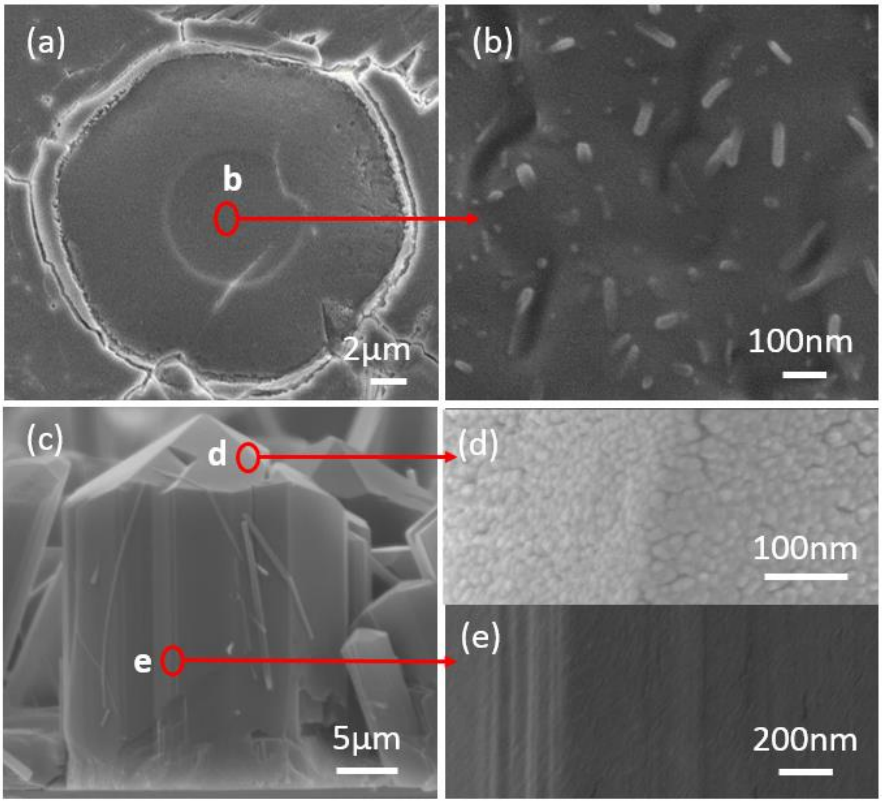

Figure 16. Close-up images of crystalline FF microstructures. (a) Top-view SEM image of a solid FF peptide seed with a roughly hexagonal shape. (b) Magnified SEM image from the circled area in a) showing nanowires leading the later growth of a FF peptide microrod. (c) Side-view SEM image of a FF peptide microrod. (d) Top view magnified image of the tip and (e) side view magnified image of the side-wall of the micro rod in (c).

The growth process is not limited by the substrate and FF peptide microrods have been successfully grown on silicon, indium tin oxide (ITO), platinum and gold, as shown in Figure 17. Again, no branches were observed in FF peptide microrods even after 12 hours of growth. However, comparing Figure 15e, which uses 6-hour growth, with Figure 17c-f, the uniformity of the microrod array seems to be degraded with prolonged growth time. This might be due to the poor control of the temperature and evaporation rate of the FF-water solution in Figure 15c, which can cause spontaneous nucleation and alter the epitaxial growth. This problem will be addressed in Chapter 3 of this thesis.

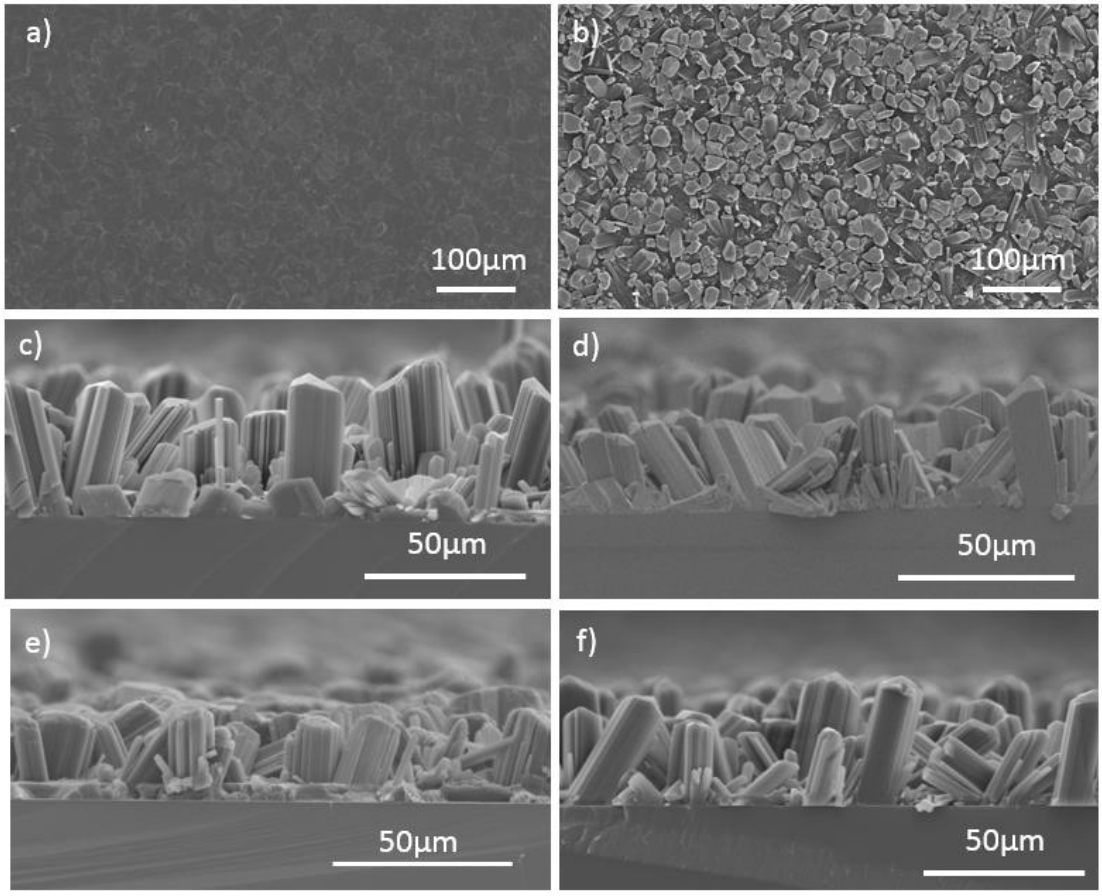

Figure 17. Growth of FF microrods on various substrates. (a) Top view of the seed layer from Figure 15d . (b) Top view of microrod array on ITO-coated silicon substrate from Figure 15e. Side views of micro rod arrays after 12 hours epitaxial growth on (c) bare silicon, (d) ITO-coated silicon, (e) platinum-coated silicon and (f) gold-coated silicon.

2.3. Insights into the seed layer formation

The highly textured and crystallized seed layer is critical for the successful epitaxial growth of FF peptide microrods, and we explore systematically the formation of FF seed layers in Figure 18a-d. In this set of experiments, 25µL FF solution of concentration either 50mg/mL or 100mg/mL was dropped and dried on a 1.25x1.25cm ITO-coated silicon

substrate to form an amorphous FF layer. Crystallization of these layers was achieved with either stationary or circulating moist air. The seed layers were examined using a Nikon Eclipse LV150 optical microscope. The scattered dark spots in Figure 18a-d are the dark ITO-coated silicon substrate revealed through vertical FF peptide domains which are good waveguides with low longitudinal optical loss [76, 79], while the bright parts are mainly horizontal FF peptide strips. We found that both the supply of water molecules during the crystallization and the thickness of the initial FF amorphous layer control the orientation of the seed layer.

Circulating moist air was proved to be critical to produce a seed layer with dominant vertical domains, as shown in Figure 18c-d. The optimal seed layer with a majority of vertical domain is obtained with 50mg/mL FF solution and circulating moist air. The highly reflective horizontal stripes become the minority in the crystallized seed

layer and most of the dark silicon substrate is visible through the dense vertical FF peptide microrods.

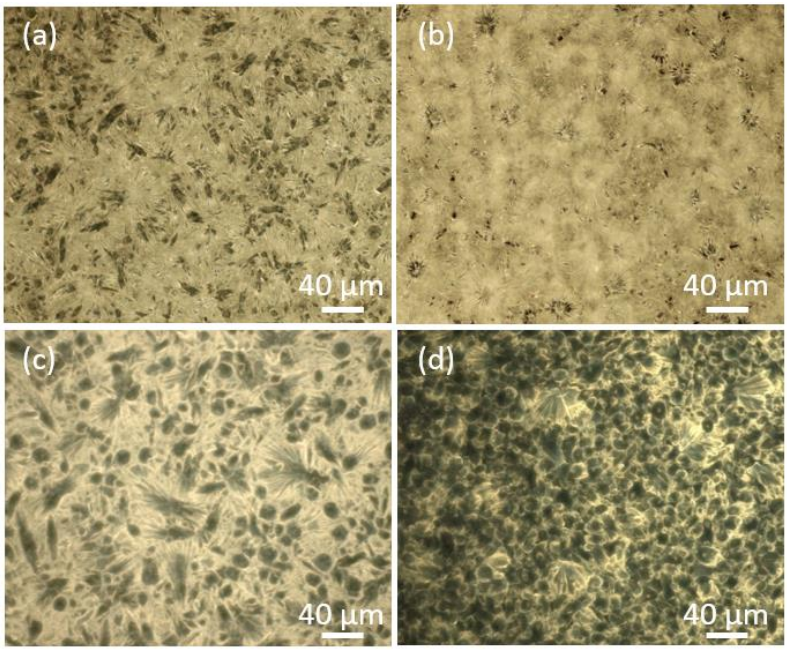

Figure 18. Optical images of the crystalline seed layer formed from different FF concentrations and moist air. (a) From 100mg/mL FF solution under stationary moist air. (b) From 100mg/mL FF solution under circulating moist air. (c) From 50mg/mL FF solution under stationary moist air. (d) From 50mg/mL FF solution under circulating moist air. All the amorphous layers used to form the crystalline seed layer were obtained by dropping 25µL of FF solution on a1.25x1.25cm square substrate.

The thickness of the amorphous layer is proportional to the concentration and the amount of FF-HFP stock solution dropped onto the substrate [65, 69], and the measurement of the amorphous layer obtained in this study confirms this trend, as shown in Figure 19a-d. Comparing Figure 18a-Figure 18c, and Figure 18b-Figure 18d, it is clear that lower

concentration, corresponding to thinner amorphous layer, yields higher portion of vertical orientation. For 100mg/mL concentration, the FF seed layer was dominated by bright horizontal FF stripes in random directions with a few transparent vertical domains which are shown as dark spots.

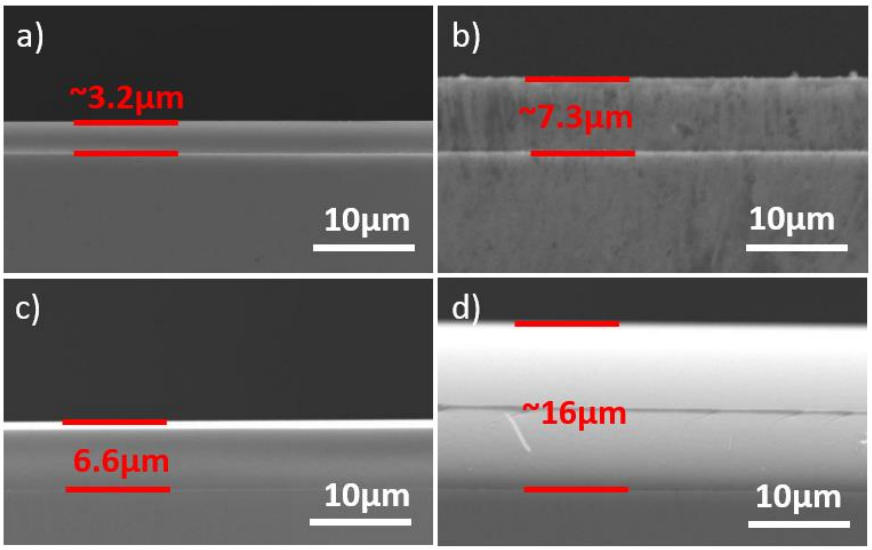

Figure 19. Thickness of the amorphous layer with respect to the concentration of the FF-HFP solution and the volume dropped on the 1.25x1.25cm substrate. (a) 25µL of 50mg/mL, (b) 25µL of 100mg/mL, (c) 40µL of 50mg/mL, and (d) 40µL of 100mg/mL.

This observation indicates that the crystallization process is driven by the diffusion of water molecules into the amorphous FF peptide layer. Fick's first law of diffusion suggests that the diffusion flux of water molecules in the vertical direction is proportional to the gradient of the concentration of water molecules, which in turn is proportional to the water vapor concentration at the surface and inversely proportional to the layer thickness. When a thick amorphous FF peptide layer is used, the water molecule diffusion normal to the substrate is limited and horizontal FF peptide strips are preferentially formed. In

comparison, the much enhanced vertical diffusion in a thin amorphous layer with continuous supply of water molecules from circulating moist air significantly facilitates the creation of vertical FF peptide microrods.

2.4. Characterization of the FF microrod array

2.4.1. X-Ray Diffraction analysis (XRD)

The crystalline structure of both seed layers and FF peptide microrods were subject to XRD analysis after they were crushed into powders and pressed on a <100> silicon substrate. XRD measurement were made using Bruker D8 system with Cobalt anode (λ=1.78899 Å). The crystal structure of FF peptide seed layers and FF peptide microrods were confirmed. Figure 20 shows typical XRD spectra of the seed layer and the FF peptide microrod. The microrod structure results in an almost identical XRD pattern to that of the seed layer. The hexagonal structure ($P6_1$ space group) proposed by Gorbitz and the resultant crystallographic data in the Cambridge Crystallographic Data Centre (CCDC) file number 163340 are in agreement with our XRD spectra [56]. The XRD data indicates the FF peptide crystals are a close-packing of nanotubes with a diameter of 24 Å. The hydrophilic nanochannels within FF hexagonal structures are deemed able to host different ions or molecules [54, 66, 80] for various applications such as energy storage or drug delivery. Consequently, the vertical FF peptide microrod with well-aligned nanochannels can increase the accessibility and transport of foreign ions or molecules.

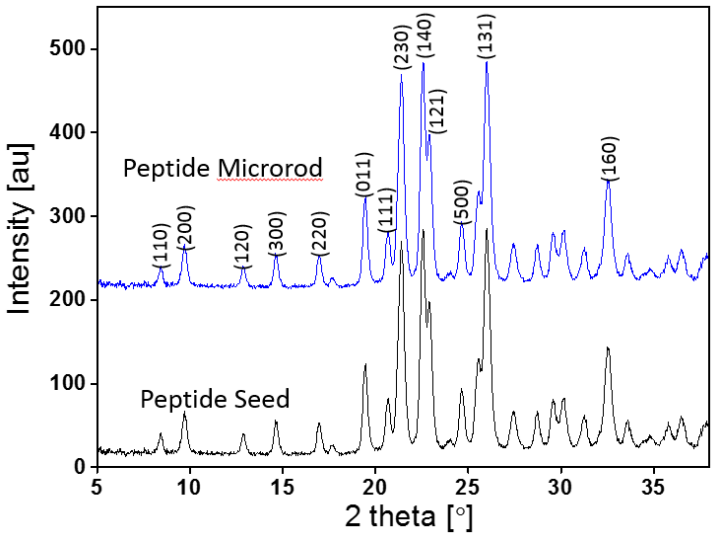

Figure 20. X-ray powder diffraction patterns of FF peptide seeds and FF peptide microrods. The spectrum of FF peptide microrod is shifted upward for clarity.

2.4.2. Piezoresponse Force Microscopy (PFM)

The highly-textured seed layer and the vertically oriented microstructures enable us to conveniently characterize their piezoelectric property using PFM, which has proved challenging to perform on free standing FF peptide nanotubes [50]. Piezoelectric coefficient measurements of the FF peptide seed layer and aligned microrods were conducted with an Asylum MFP 3D system. The probe used was an Asylum Research ASYELEC-01 with Ti/Ir conductive coating, nominal stiffness of 2N/m, and nominal resonance frequency of 70kHz. To measure effective piezoelectric coefficient d_{33}, a small area (0.5x0.5μm) was scanned in Single Frequency Mode with very low frequency (10kHz) to avoid contact resonance (typically around 300kHz). Drive voltage amplitude on the tip varied from 2V to 14V and the corresponding vibration amplitude of the tip was recorded and averaged over the scanned small area to calculate d_{33}. The amplitude responses of the

PFM measurement on the peptide seed and on the FF peptide microrod are shown in Figure 21. The amplitude increases linearly with the applied voltage, and the slope gives the effective piezoelectric coefficient $d_{33} = 9.4$ pm/V for the FF peptide seed and $d_{33} = 9.9$ pm/V for the FF peptide microrod.

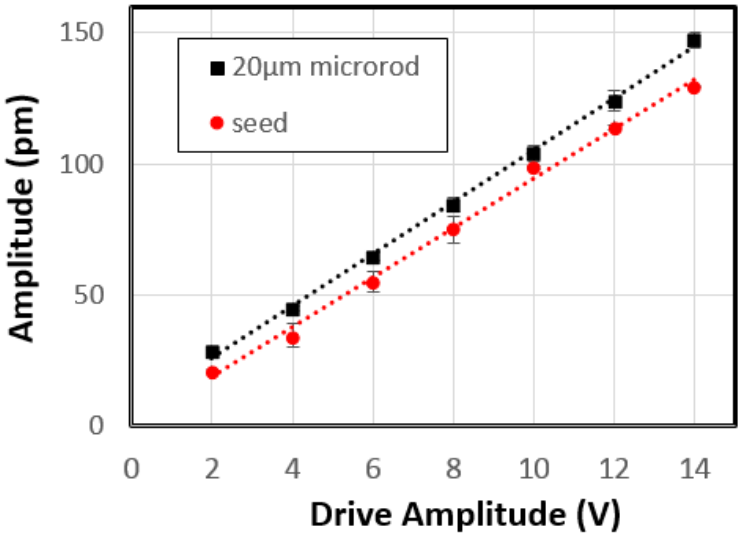

Figure 21. PFM amplitude response of an FF peptide seed layer and FF peptide microrods.

This result indicates that the longitudinal piezoelectric coefficient d_{33} of FF peptide microrods is comparable to that of ZnO nanowires [21], and the vertically aligned array of FF peptide microrods can potentially be a good candidate for mechanical energy conversion applications.

2.5. Chapter summary

In this chapter the low temperature fabrication of densely packed, vertically aligned FF peptide microrods was demonstrated. The crystal structure of FF peptide microrods

with hexagonally arranged nanochannels was confirmed with XRD. The effective longitudinal piezoelectric coefficient d_{33} of 9.9 pm/V was measured with PFM. The high quality piezoelectric biomaterial from this work provides a new platform for applications in sensing, energy harvesting, and medicine.

CHAPTER 3. CONTROL OF POLARIZATION OF FF PEPTIDE MICROROD ARRAY FOR PIEZOELECTRIC NANOGENERATOR

3.1. Observations of the inherent polarization in FF crystals

Strong piezoelectricity has been measured in FF hexagonal crystals, which was demonstrated in [50] and in Chapter 2, thanks to the inherent polarization orienting along the nanochannels. Realizing macroscopic piezoelectricity in FF crystals requires uniform polarization with good alignment of their inherent electrical dipoles in the desired orientation. Although significant progress has been made towards the synthesis of piezoelectric biomaterials and their applications, challenges in aligning the polarization and improving the piezoelectricity continue to limit their applications. Various strategies have been developed to obtain alignment, such as molecular self-assembly [71, 81, 82], template-assisted assembly [44, 83] and ferrofluid-assisted assembly [71]. However, most of the processes were relatively complex to scale up and could not be effectively used to achieve parallel polarizations. Like antiparallel dipole moments observed in M13 phages [43, 44], the oppositely directed polarizations were revealed in adjacent FF peptide nanostructures [50, 84]. Although ferroelectric behavior has been observed for FF nanotubes through high-temperature treatment, the polarization was only switched in the radial direction while the axial polarization was destroyed due to an irreversible phase transition to the centrosymmetric structure [85]. The high coercive field in the axial direction leaves native FF crystals practically un-switchable before electrical breakdown [60].

Lack of macroscopic piezoelectricity limits the development of FF for piezoelectric device. A microbeam resonator based on FF microtube has been demonstrated, but it was not a standalone device, requiring AFM probe as an actuator, as shown in Figure 22. Piezoelectric devices based on other biomaterials have also been investigated, such as virus-based nanogenerator [43, 44], but their anti-parallel polarizations and weak piezoelectric coefficients significantly limited their performance.

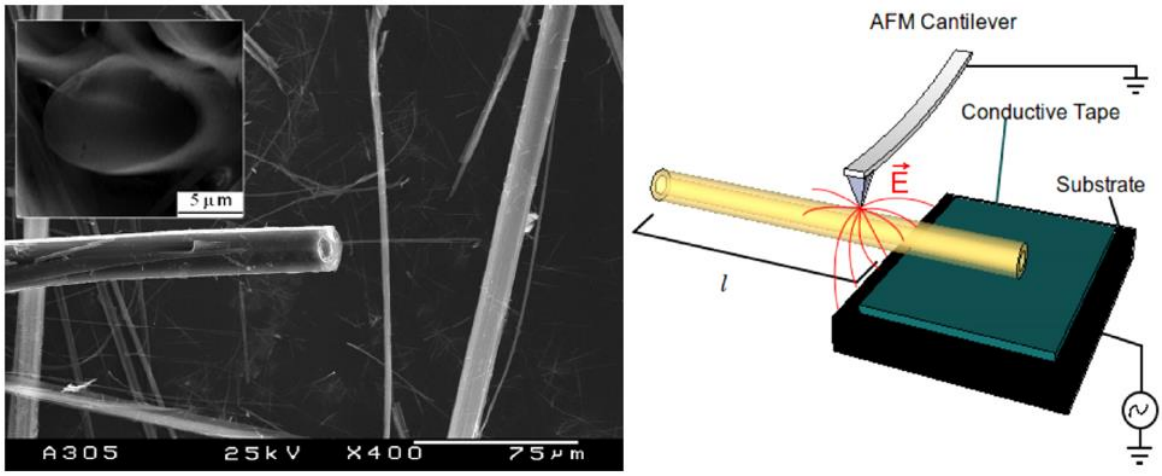

Figure 22. An FF microtube resonator actuated by AFM probe [86].

3.2. Control of polarization of FF microrod array with improved piezoelectricity

3.2.1. Modified epitaxial growth of FF microrod array

The vertical FF peptide microrods were grown from a substrate coated with a seed film in an FF-concentrated water solution, with two modifications from Chapter 2.

(1) In the epitaxial growth in saturated FF-water solution, the temperature is now elevated to 55ºC from start to finish, and the water evaporation rate is limited by partly covering the water surface exposed to air. The higher temperature

enables higher saturated FF concentration and faster growth, while limiting water evaporation prevents spontaneous nucleation in the solution for better uniformity.

(2) An electric field was applied either along or opposite to the substrate surface normal, and the corresponding growth processes were called positive-EF (electric field) growth and negative-EF growth, respectively, as shown in Figure 23a-b. The electric field is applied to control the polarization of the microrod array.

In positive-EF, negative-EF, and no-EF growth, positive, negative, and no electric fields were applied respectively during the self-assembly of FF peptides. The voltage was provided across two aluminum plates (15×15 cm^2) by a high-voltage generator (Glassman High Voltage, Inc., model PS/MJ1OP1500-11). 5 kV across a 5 mm gap and 8 kV across a 4 cm gap were used in seed fabrication and solution growth, respectively. The seed film was prepared, in similar steps as in Chapter 2, by drying a 20 μL drop of 1,1,1,3,3,3-hexafluoro-2-propanol (HFP) (Sigma Aldrich) with FF peptide (Bachem) at a concentration of 45 mg mL^{-1} on a 1.25×1.25 cm^2 gold-coated silicon substrate. The stock materials were all stored in enclosed containers to minimize undesired water absorption from the environment. The obtained amorphous film was crystallized into vertical microrod domains by vigorously circulating 100% humid air for 60 seconds.

Then an FF-water solution was prepared by dissolving FF peptide in water to 2 g L^{-1} concentration at 70°C. The dissolution process was monitored so that the resulting

solution was completely clear. 5 mL of FF-water solution was then distributed into a 40 mm-diameter petri dish, which was placed between the two 15×15 cm^2 aluminum plates, in an oven at 55°C. The substrate with seed film was put upside down floating on the FF-water surface. The petri dish was covered by a lid with five 5 mm-diameter holes that limited the water evaporation rate and suppressed spontaneous nucleation in the FF-water solution. After 6 hours of growth, the substrate was taken out and the residual water was blown off with compressed air.

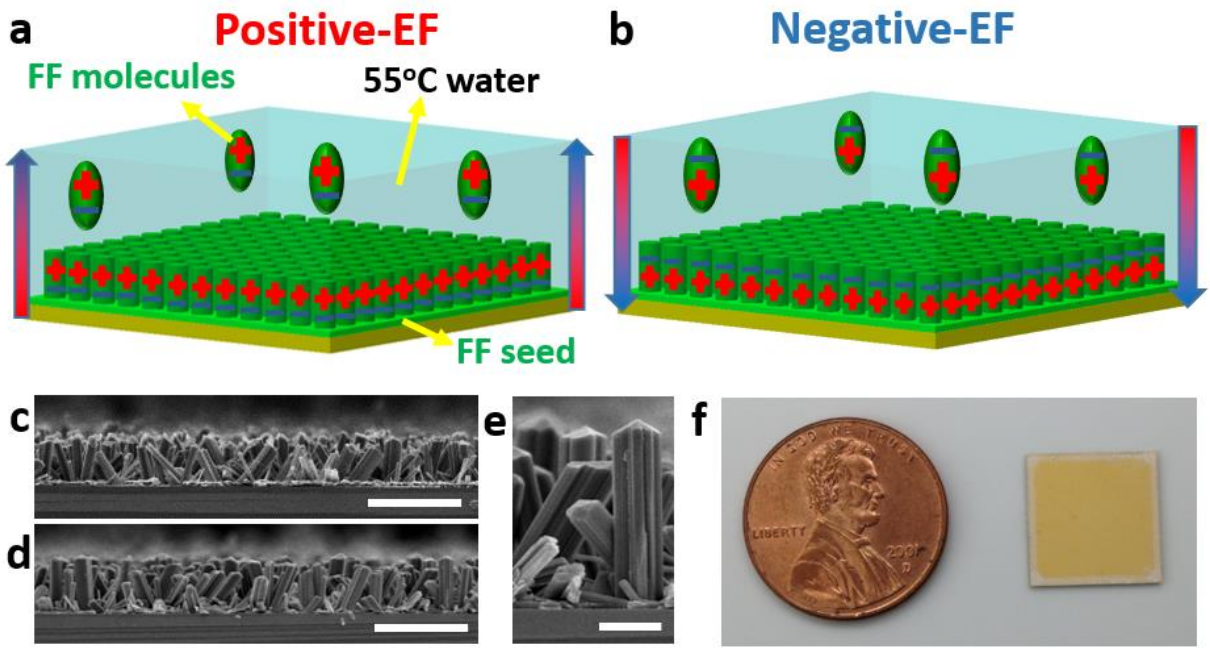

Figure 23. Growth of vertical FF peptide microrods arrays with controlled polarization. (a,b) Schematic of the positive-EF (electric field) growth (a) and the negative-EF growth (b). The large arrows are the directions of the applied electric fields, and the plus and minus signs indicate the polarizations of the FF molecules and FF microrods. (c,d) Cross-section views of arrays from the Positive-EF growth (c) and the Negative-EF

growth (d). Scale bars in (c) and (d) are 100 µm. (e) High-magnification view of vertical microrods. Scale bar is 20 µm. (f), Photography of vertical FF peptide microrod array grown on a gold-coated substrate. The yellow gold layer is visible owing to the vertical alignment of microrod arrays and good optical waveguide properties along their axial directions.

As shown in Figure 23a-b, The mobile FF molecules in the solution were aligned so that their electrical dipoles were along the applied electric field during the FF peptide self-assembly [87]. The orientation of the FF molecules being deposited onto the seed determined the polarization of the microrods. Thus, the polarizations of the microrods were in the same direction as the applied electric field, and the spontaneous polarization should result in surface charges on the tips of microrods. Meanwhile, electric fields did not significantly affect the morphology of the microrods, as shown by SEM cross-section images in Figure 23c-e and top images in Figure 24a-b. The length of the microrod grown after 6 hours is increased up to about 50 µm, compared to only 10-15 µm grown in room-temperature. Figure 23f shows uniform FF peptide microrod arrays grown on a 1.25×1.25 cm^2 gold-coated silicon substrate. Since FF peptide microrods are a good optical waveguide axially but poor light transmitter radially [79], the visibility of the yellow gold film provides an easy way to confirm the good vertical alignment of the microrod arrays (Figure 23f and Figure 24c).

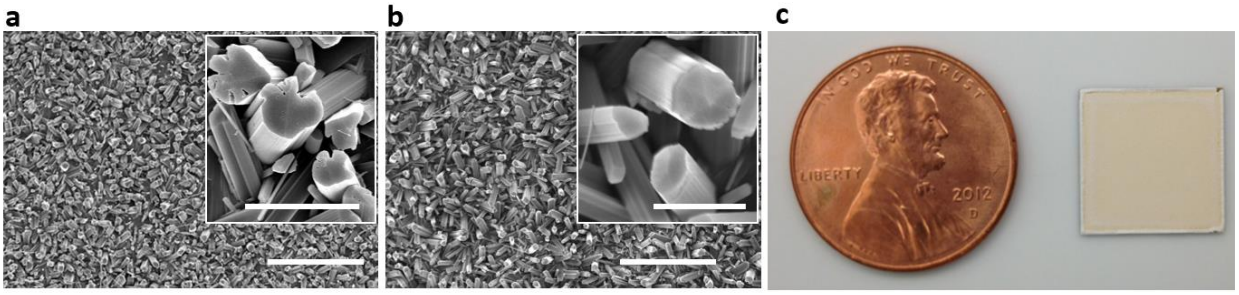

Figure 24. Top view SEM images of FF microrods array. (a,b) Top view of the microrod arrays from the positive-EF growth (a) and negative-EF growth (b). Insets: enlarged view of microrods. The scale bars in low-magnification images are 200 µm, and the scale bars in insets are 20 µm. (c), A gold-coated substrate with mostly horizontal peptide microrods. The gold layer electrode is hardly visible owing to the poor light transmission in the radial direction of FF peptide microrods.

The X-ray diffraction spectra (Figure A1 in Appendix) confirms a hexagonal crystal structure with the space group $P6_1$, similar to the structure obtained from room-temperature growth in Chapter 2.

3.2.2. Characterization of polarization control and piezoelectricity

To investigate the orientation of electrical polarization, Dual AC Resonance Tracking Piezoresponse Force Microscopy (DART-PFM) and Scanning Kelvin Probe Microscopy (SKPM) with an Asylum MFP 3D system was conducted on the top of the FF peptide microrods to measure phase response and surface potential, respectively. Using DART-PFM to determine the phase responses of the array can reduce noise and topography crosstalk compared to single frequency technique. The probe used in both modes was an

Asylum Research ASYELEC-01 with Ti/Ir coating on both cantilever and tip. The nominal resonance frequency of the probe was 70 kHz, and the tip radius was 28±10 nm according to the manufacturer. In all PFM scans the probe was typically pressed on the sample surface with a force of about 100 nN. The inverse optical lever sensitivity (InvOLS) and spring constant were calibrated before all measurements using Asylum's software GetReal. The probe was excited at 1 V amplitude and contact resonance frequency was typically ~300 kHz. Correction for the instrumental phase offset was done by shifting the phase responses so that the phase at contact resonance was 90˚. In SKPM the dual-pass technique was used. In the first pass for detecting topography, the set point was 65-70% of free amplitude (~100 nm), and the tip was lifted 50 nm above the surface in the second pass for measuring surface potential.

As an alternating voltage on the FF peptide microrods was applied, an FF peptide microrod with either upward or downward polarization deformed either out of phase (180^o) or in phase (0^o), respectively (Figure 25a-b and Figure A2 in Appendix). The phase distributions of vertical microrods from a positive-EF growth and from a negative-EF growth in Figure 25a-b, respectively, show that applying opposite electric fields during growth results in FF peptides with phases of polarization 180^o apart. SKPM confirmed that the surface charge of the microrod tip was consistent with the polarization, verifying the mechanism shown in Figure 23a-b.

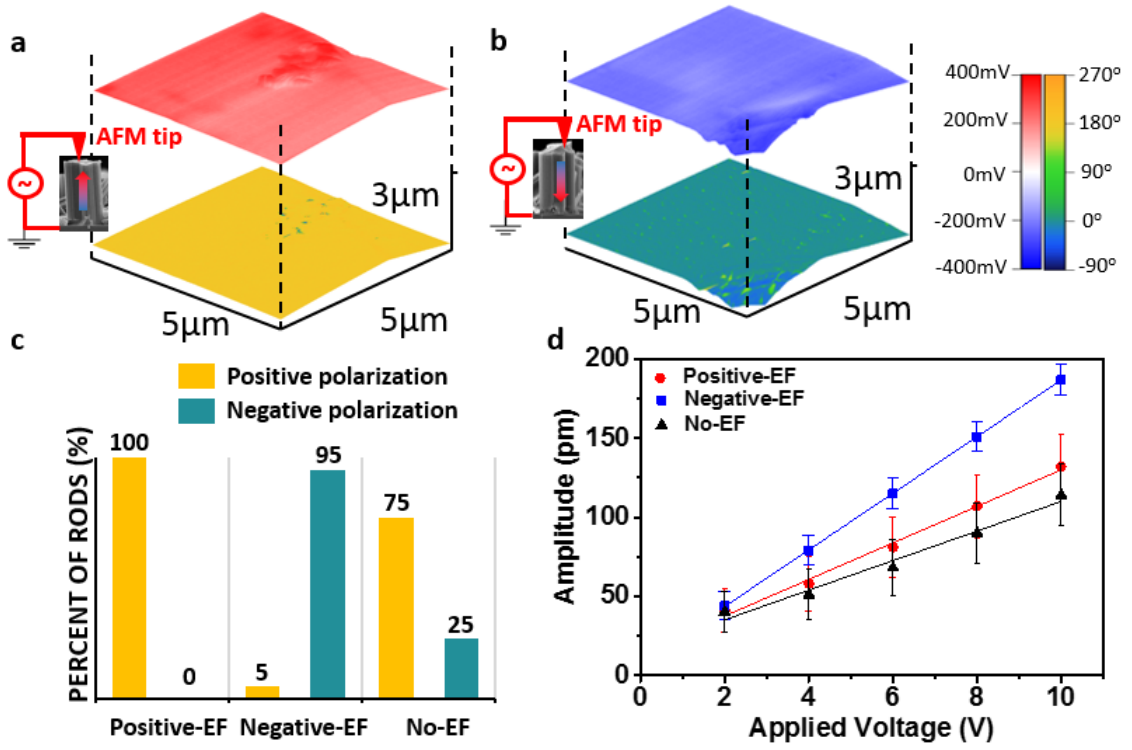

Figure 25. PFM and SKPM characterization of the microrod arrays. (a,b) PFM phase image and corresponding SKPM surface potential map of a microrod from the positive-EF growth (a) and a microrod from the negative-EF growth (b). The phase and surface potential distributions are shown by the color overlaid on the topography of the top of the microrod. (c) Statistics of the piezoelectric phase for the arrays from the positive-EF growth, negative-EF growth, and no-EF growth. Detailed data for this chart is provided in Appendix Table A1. (d) Linear dependence of the PFM amplitude on the applied voltage for FF peptide microrods from growth with different electric fields. The slopes of the lines provide effective piezoelectric coefficients d_{33}, which are 17.9 pm V^{-1}, 11.7 pm V^{-1} and 9.3 pm V^{-1} for microrods from the negative-EF growth, positive-EF growth, and no-EF growth, respectively.

20 random microrods from each growth process were tested (Figure 25c and Appendix Table A1). The tested 20 microrods were randomly selected at four 1×1 mm^2 sites on the substrate, and were at least 200 μm apart. The results indicated that 95-100% of microrods had polarization in the direction of the applied electric field. In the absence of an electric field during growth, the polarization distribution became much less uniform (Figure 25c). A preferential polarization was often observed in such no-EF growth, which might have been due to native charges on the substrate or even small electric fields from surrounding equipment [58, 80, 87]. The inherent polarization of FF peptides originates from the ordered arrangement of positively charged amino termini (NH_3^+) and negatively charged carboxyl termini (COO^-) [58]. Therefore, microrod arrays with opposite polarizations have either NH_3^+ groups or COO^- groups predominantly exposed at the top surface. Hence, the biofunctionality of the FF peptide microrod array can be tuned by simply switching the electric field during growth.

The piezoelectric strength of vertical microrod arrays was examined by measuring their effective piezoelectric constant d_{33} (Figure 25d). To determine d_{33}, Single Frequency mode was used and the probe was excited at 20 kHz, which is far from contact resonance to avoid signal amplification. An area of 500×500 nm^2 was scanned under AC voltages between 2 V and 10 V. The average vibration amplitudes in each scanned area were recorded to calculate the effective d_{33}. The highest effective piezoelectric constant d_{33}=17.9 pm V^{-1} was observed from this study, much higher than the value of 9.9 pm V^{-1} obtained from room-temperature growth. The improved piezoelectricity is ascribed to a better alignment of FF peptide molecular dipoles assisted by the electric field and elevated

temperature. The result is consistent with a recent theoretical study which shows that an external electric field stretches the peptide backbone of the FF molecule and significantly increases the dipole magnitude [87]. The temperature determines the number of water molecules in an FF peptide hexagonal crystal, and hence, the lattice constants and piezoelectricity [60, 85, 88]. However, further investigation on the effect of the electric field and temperature is needed to provide more insights.

In order to realize macro-scale piezoelectricity, the high piezoelectric coefficient needs to be combined with the control the polarization over the whole array, because the polarization is very stable and could not be switched with a high electric field once the growth is completed, as shown by the hysteresis loop in Figure 26. This observation verifies the significance of the growth process described in this section in realizing the piezoelectric device in the next section.

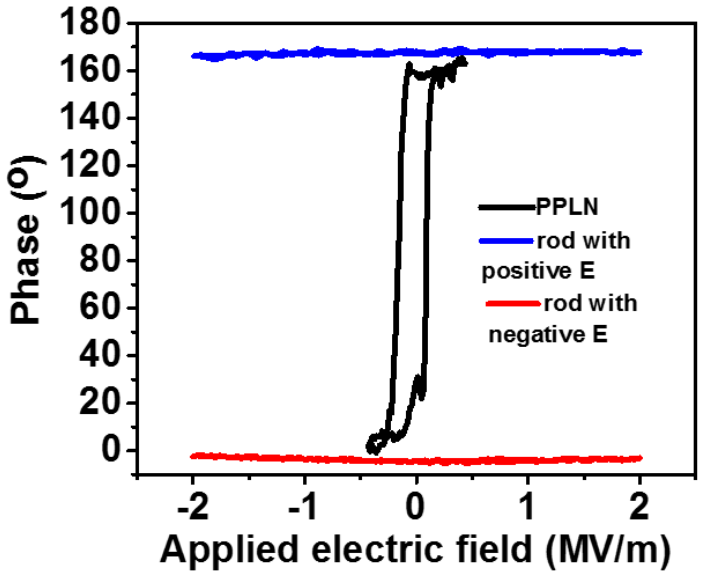

Figure 26. Hysteresis loop measurements of FF peptide microrods. The control sample is a standard periodically poled lithium niobate (PPLN, Asylum Research). Compared to the PPLN, FF peptides have a much higher coercive field. Both the positive and negative polarizations were confirmed to be stable under high electric field. The polarizations could not be switched before the material was destroyed from electrical breakdown.

3.3. Piezoelectric nanogenerator based on FF microrod array

We investigated the power generation using FF peptide microrods with controlled polarizations. The FF peptide microrod array was sandwiched between two electrodes that connected to an external load or measuring instruments, as shown in Figure 27a. When the device was compressed and released, FF peptide microrods converted the mechanical energy into electricity. The device characterization setup in Figure 27b includes a closed-loop linear motor (E100-RD-HC type with Force Control, LinMot) with a load cell (FC2231, Digi-Key) mounted on the tip. A periodic compressive force was applied on the

power generator for 1 second and released for 2 seconds. Devices from all polarization scenarios were systematically measured, in which at least 5 cycles were run for each voltage, current and power data point before average values and errors were calculated. A minimum (5 N) force was maintained during the test to avoid creating an unintentional triboelectric effect due to the separation of the generator and the actuator. Thus, the applied force was the difference between 5 N and the peak force. The outputs of the generator were recorded using an electrometer (Keithley 6517B) and a current amplifier (Keithley 428). The generator was characterized in a Faraday cage to avoid interference from the surrounding equipment, and the linear motor was placed outside of the cage.

The power generation of FF peptide microrods from positive-EF growth is shown in Figure 27c-d. Under an applied force F=60 N, the output open-circuit voltage (V_{oc}) and short-circuit current (I_{sc}) reached 1.4 V and 39.2 nA, respectively. FF peptide microrods from negative-EF growth produced opposite voltage and current outputs, and FF peptide microrods from no-EF growth produced much smaller output (Appendix Figure A3). The signs of open-circuit voltage and short-circuit current under compressing force all agree with the polarization direction measured from PFM. Reversed connection tests show that all outputs are reversed (Appendix Figure A4). The switching-connection test excluded the errors from the variation of contact resistance or parasitic capacitance and confirmed that the detected electrical signal was truly from the piezoelectric FF peptide microrods. Unlike generators based on virus or zinc oxide nanostructures, which showed rapid decay of the open-circuit voltage due to the leakage current through these materials [34, 43, 44], the

open-circuit voltage herein remained at a constant level owing to the excellent dielectric properties of FF peptides [89] (Appendix Figure A5).

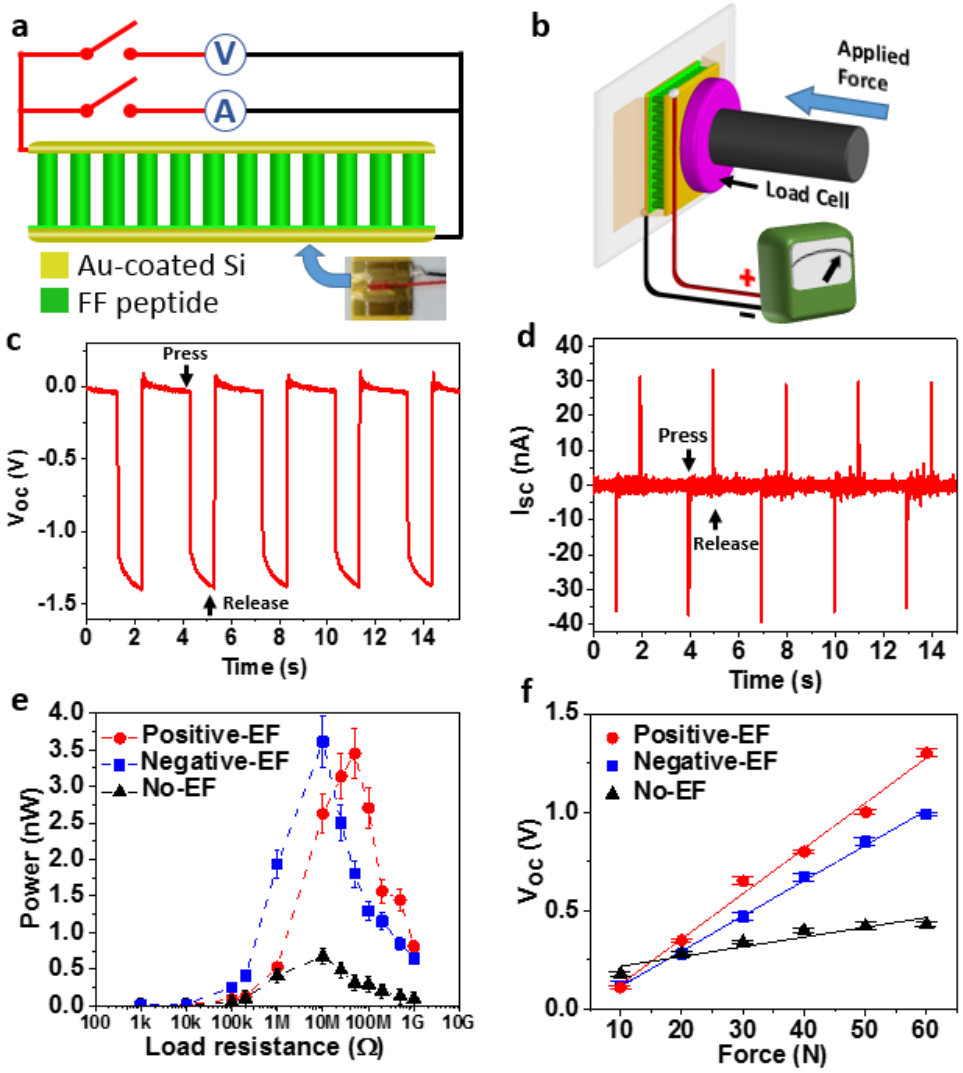

Figure 27. Characterization of the FF peptide-based power generators. (a) Schematic of the FF peptide-based generator connected to the measurement equipment. Bottom-right inset: photography of a real device. (b) Schematic of the measurement setup in which a linear motor pushes with controlled forces on the top electrode in (a). The linear motor

was programmed to always keep contact with the top electrode to minimize the effect of static charges. (c,d) Open-circuit voltage (c) and short-circuit current (d) from a generator using microrods from positive-EF growth. (e) Dependence of the power output from the generators on the resistance of the external load under 50 N applied force. (f) Linear dependence of the open-circuit voltage on the applied force.

When connected to external resistors, FF peptide microrods grown with electric fields produced up to 3.3 nW cm^{-2} at 50 MΩ, which is 3.8 times higher than the power density of zinc oxide nanowire-based generators (0.854 nW cm^{-2} for a single generator) driven by a 24 times greater pressure [34]. Our comparison here is conservative since the reported vertical zinc oxide nanowire-based generator was not connected to a real load, so its power output was estimated using separately measured peak voltage (96 mV) and current (8.9 nA cm^{-2}), which cannot be achieved simultaneously. In contrast, FF peptide microrods grown without electric fields yield power about 5 times lower than the power produced from microrods grown with electric fields (Figure 27e), demonstrating the importance of the applied electric field for output enhancement. The Effect of strain rate on the output of FF peptide-based generators was also investigated, and increasing strain rate was found to increase the peak power output up to 7 nW cm^{-2} (Appendix Figure A3e), which was comparable to the performance of a generator based on lead zirconate titanate (PZT) nanoribbons [90].

Time-integration of current peaks yields an average charge Q=530 pC (Appendix Table A2 and Figure A6). In the quasi-static case, the relation $d_{33}=Q/F$ holds [91], from

which we obtain an estimated piezoelectric constant $d_{33} \approx 8.8$ pm V^{-1}. It is smaller than the effective piezoelectric constant measured by PFM, indicating that not all microrods contribute to the power generation and that the device can be further optimized. The linear piezoelectricity of FF peptides was verified by the linear dependence of the V_{oc} and I_{sc} on the applied force (Figure 27f and Appendix Figure A3f).

To further verify the authenticity of the FF peptide-based generator, control experiment was performed by replacing the FF peptide microrod array with a non-piezoelectric Kapton thin film. The output signals became negligible (Figure 28), further validating the output of the generators.

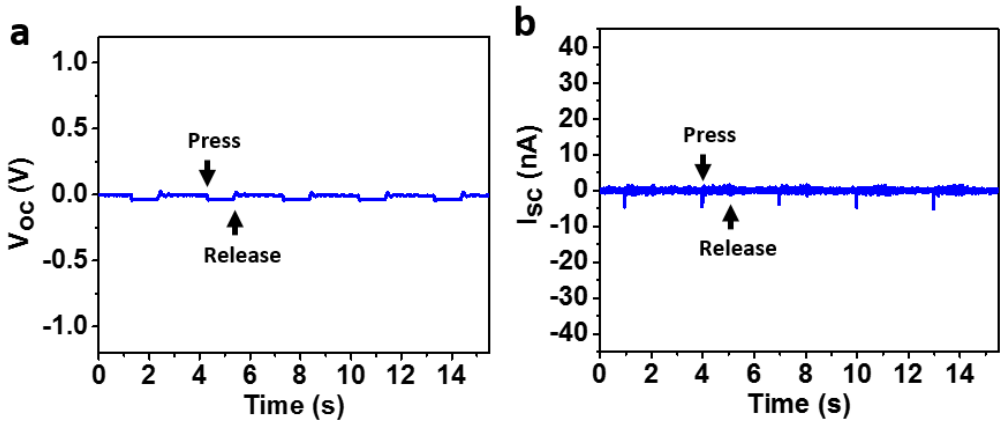

Figure 28. Power output control measurement for FF peptide-based generator. (a,b) Open circuit voltage (a) and short-circuit current (b) of a control device in which the FF peptide microrod array was replaced by a 50 μm-thick non-piezoelectric Kapton film.

The fatigue behavior of the FF peptide-based generator was evaluated. We tested the V_{oc} of a generator under a cyclic force (50 N) for an extended period of time (Figure 29a-b). The output voltage showed no degradation over more than 1,000 press/release

cycles for more than half an hour. We repeated this test 5 times on the same device for a total of over 5,000 cycles and the device did not show any degradation, indicating the high durability of FF peptide-based devices. Finally, by stacking three power generators on top of each other, we were able to further increase the power output and directly drive a seven-segment liquid crystal display (LCD) (Varitronix VI-201-DP-RC-S, Digi-Key). The letters of "FF" on the LCD were activated when the generator was pressed by a human's finger (Figure 29c-e), demonstrating the capability of the FF-based power generator to harvest biomechanical energy.

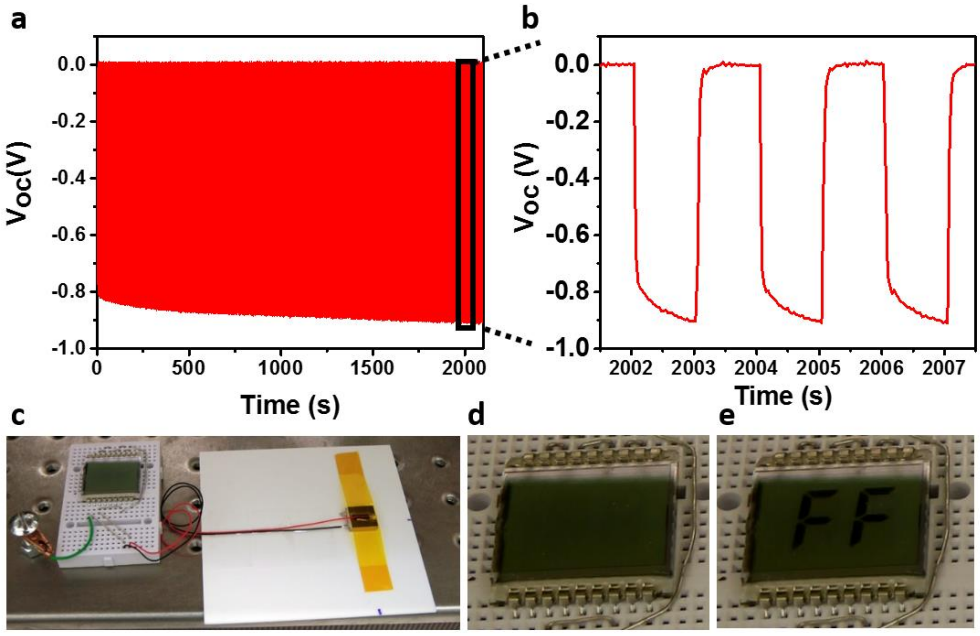

Figure 29. Demonstration of the FF peptide-based generator as a practical power source. (a,b) Open circuit voltage over time as the generator was pressed under 50 N force for over half an hour at 0.5 Hz (a), and the enlarged view of the voltage output (b). The time was limited by the storage of our measuring instrument. The background shift due to long

time measurement was subtracted from the recorded signal for clarity. (c) Photograph of the generator as a direct power source for an LCD. (d,e) Photograph of the LCD before (d) and after (e) the generator in (c) was pressed by a human finger.

3.4. Chapter summary

In conclusion, we have obtained vertical FF peptide microrods with controlled inherent polarization and improved piezoelectric strength. The microrod arrays were used to fabricate a power generator whose power density substantially exceeded that of similar devices. The output was increased with stacked generators and an LCD could be driven as the device was pressed by a finger. The uniform polarization in two opposite directions promises to expand the applications of FF peptide beyond energy harvesting and piezoelectric devices. Our present study on FF peptide power generators is a significant step toward developing FF peptide into a smart, versatile, and biocompatible material platform.

CHAPTER 4. TRIBOELECTRIC NANOGENERATOR AND THE ENVIRONMENTAL EFFECTS ON ITS OUTPUT

4.1. The role of surface patterns and adsorbed water layer on triboelectrification

In 2012 the first triboelectric nanogenerator (TENG) was invented utilizing the triboelectrification between two untreated polymer surfaces and electrostatic induction to generate current flow through external circuit [25]. The schematic of the working mechanism of the TENG is shown in Figure 30.

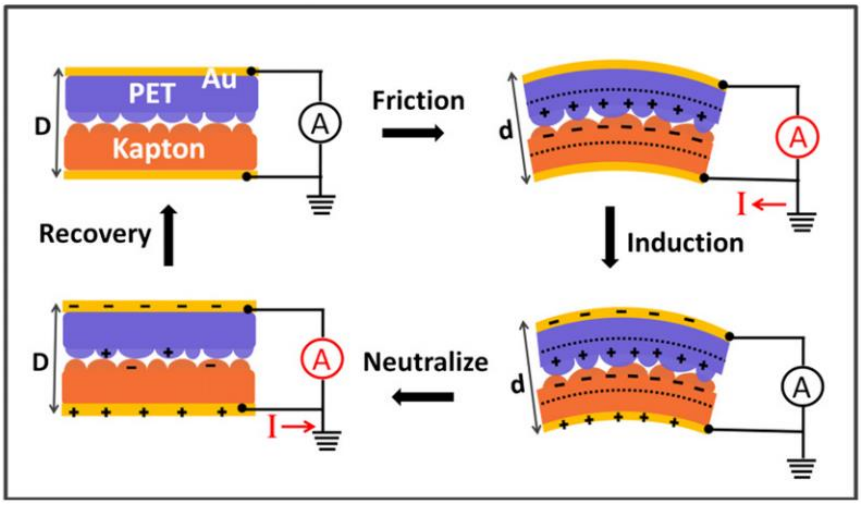

Figure 30. The first flexible triboelectric nanogenerator utilizing two unmodified polymer thin films [25].

Since TENG relies mainly on friction, there have been significant studies on fabricating surface structures to enhance the contact surface area, and thus charge generated. Various micro/nanostructures have been fabricated and tested for TENG, and

they were proved to produce higher output than the untreated flat films, as shown in Figure 31 [92].

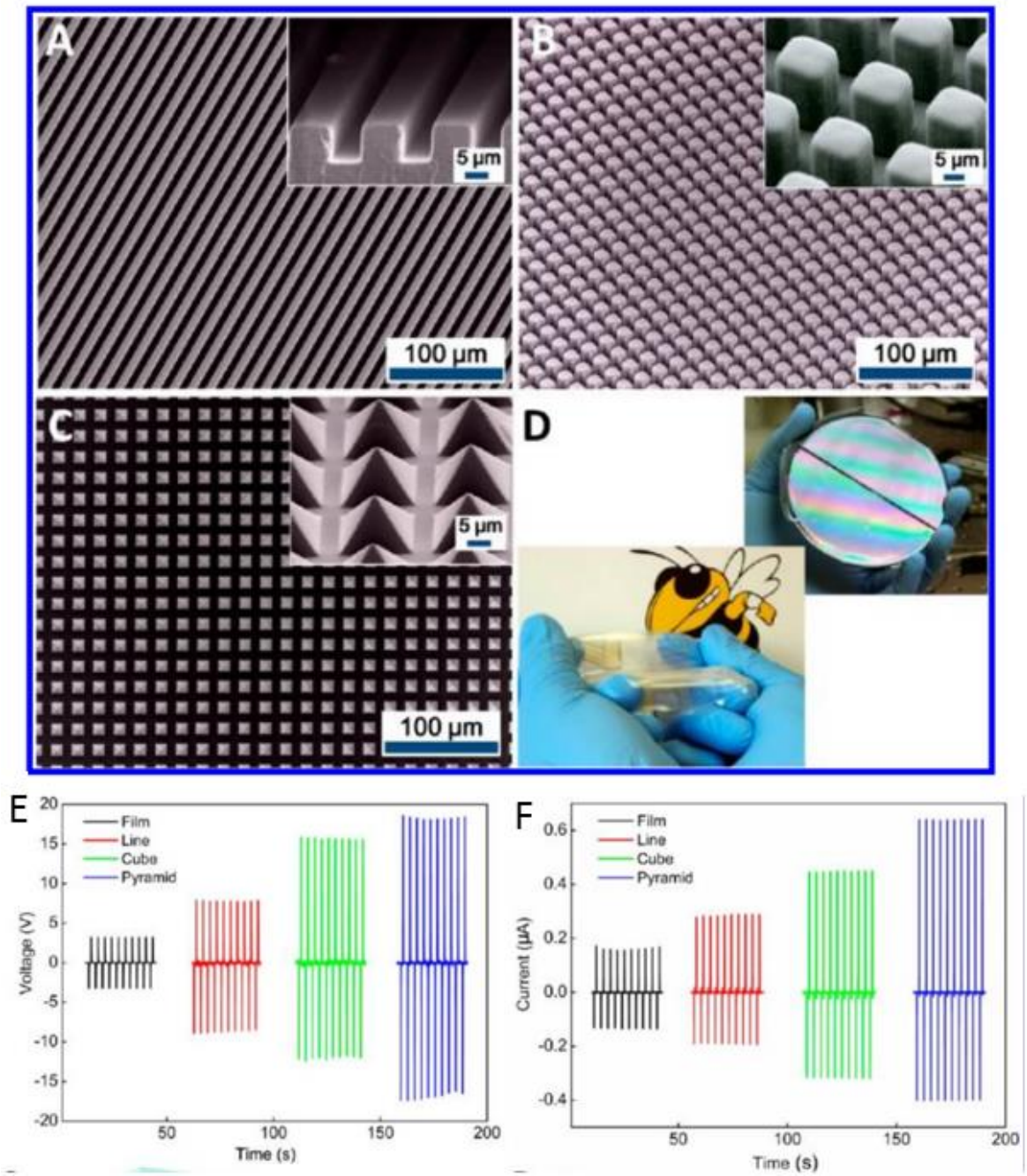

Figure 31. Effect of micro lines, cubes and pyramids on the output of TENG [92].

Environmental parameters such as relative humidity (RH) has been known to take effect on triboelectrification by governing the "water bridge" layer that adsorbs onto the material's surface, illustrated in Figure 32 [93, 94]. This adsorbed layer is suggested to contribute to the transfer of ions which can be either native ions in the polymer or hydroxyl groups in water [95]. Experiments have been conducted to answer the question of whether or not increasing RH would increase the amount of charge transferred [93, 95], or even if water is necessary at all. In other experiments [14], contact charge is still observed between metals and polymers at 1 μTorr [96], and between insulators at 5 Torr [97], indicating a wide application range of the triboelectric effect at different pressure. However, the results have been inconclusive and there is no overall trend of the effect of environmental factors for all materials.

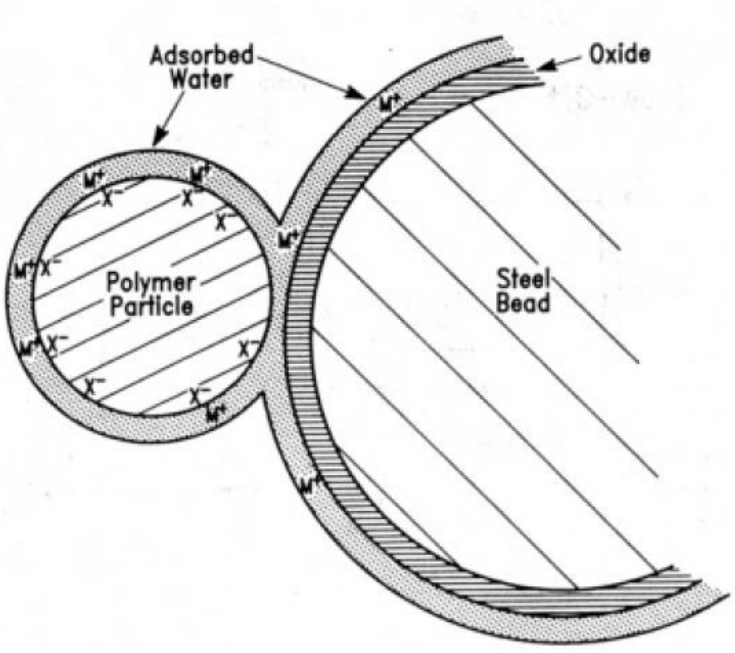

Figure 32. The water bridge between polymer and metal particles upon contact. [93]

4.2. Surface patterning and TENG design

4.2.1. Surface patterning

Among the surface materials reported for the triboelectric effect, aluminum and poly(dimethylsiloxane) (PDMS) are of special interests due to their highly opposite positions in the triboelectric series [35]. Their low-cost and good manufacturability at micro/nano scale also make them very suitable for triboelectric effect studies [98-101]. In this section a TENG will be constructed from PDMS and aluminum contact pair enhanced by surface micro patterns.

First the micro pyramids are fabricated for both aluminum and PDMS surfaces to enhance the charge generated during triboelectrification. Although micro pyramids show better performance than other photolithography-based microstructures, and have been employed in numerous studies of TENG, they are mostly fabricated on only polymer surface [92, 99, 101]. In order to obtain the micro pyramids for the metal surface, a simple process was developed to produce a positive silicon mold shown in Figure 33a on the left column. The <100> silicon wafer was first dry-etched in O_2 and SF_6 to obtain vertical 20x20 μm^2 square columns about 15μm tall. The wafer then continued to be wet-etched in potassium hydroxide (KOH) at 70^oC for about 4 minutes so that the square columns were etched into positive pyramids. Lastly, 150nm of aluminum layer was deposited onto the positive-pyramid silicon mold to obtain the metal electrode of TENG. Pyramids on PDMS was fabricated using typical soft lithography process which utilized a negative silicon mold, also shown in Figure 33a. The micro pyramid structures were successfully fabricated

on a 20x20mm^2 for both aluminum and PDMS surfaces, and their SEM images are shown in Figure 33b-c.

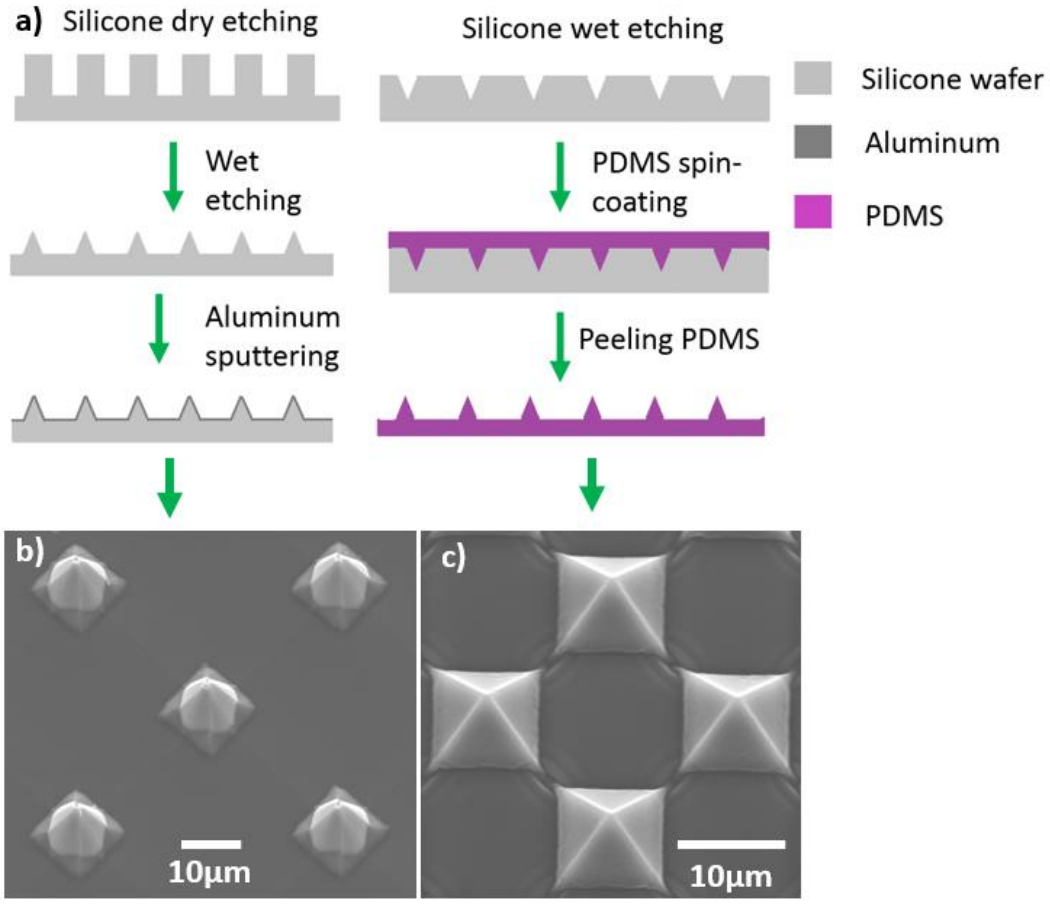

Figure 33. Patterning of micro pyramids for aluminum and PDMS. (a) Schematics of the processes used to produce micro pyramid structures for aluminum and PDMS surfaces. SEM images of (b) Aluminum-coated silicon pyramids and (c) PDMS pyramids.

4.2.2. TENG design

As opposed to the widely popular arch-shaped and flexible-electrode TENG structure [99, 101], in this study a rigid planar structure will be designed to ensure

repeatable and complete contact between the two surfaces. The TENG consisted of aluminum and PDMS electrodes, a spacer, a flexure, and a base, as shown in Figure 34a.

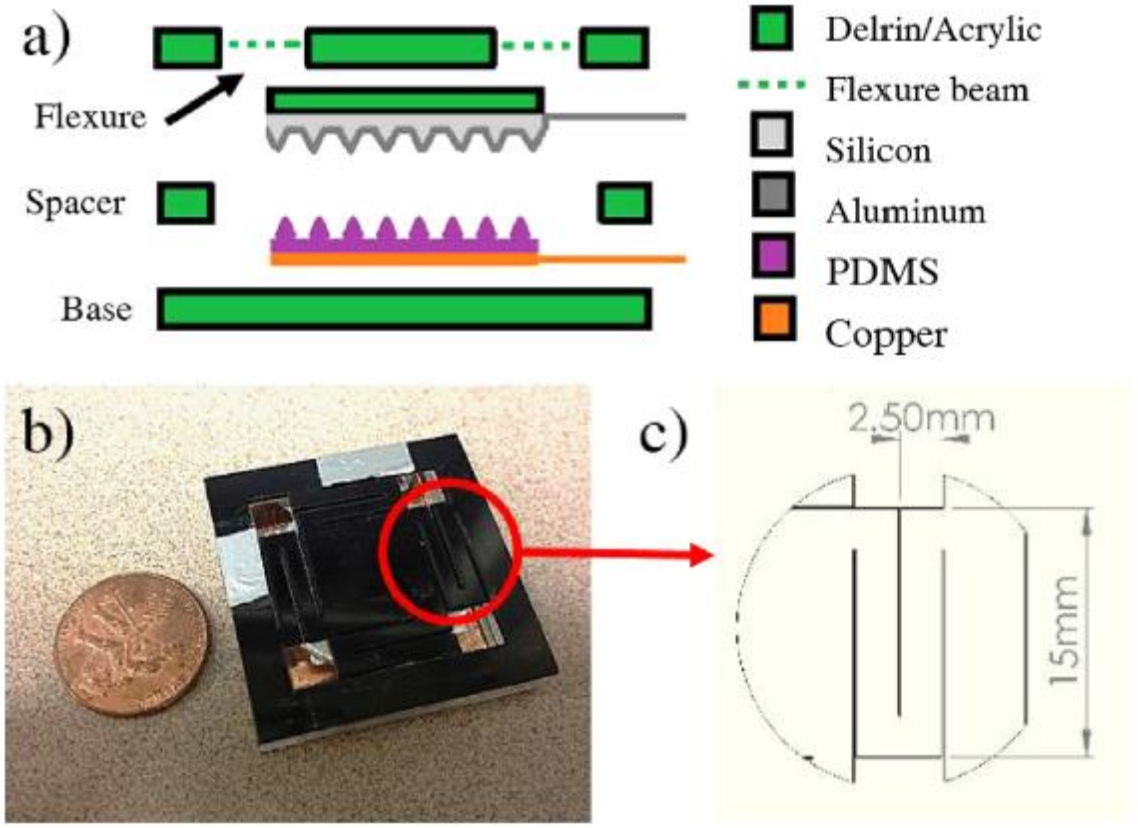

Figure 34. Structure of fabricated parallel-plate TENG. (a) Schematic diagram of the TENG, (b) optical image of a real device, and (c) structure of the flexure with dimensions,

The out-of-plane flexure structure was designed and fabricated to enable repeatable contact and separation between the aluminum and PDMS surfaces. The flexure was made from a commercial Delrin (Polyoxymethylene) thin sheet (0.8mm thick), and the spacer and the base were made of acrylic. These plastic parts was fabricated by laser cutting. The

length, width and thickness of the flexural beam need to be well designed for a suitable stiffness which is high enough for the device to easily spring back after load and low enough to efficiently respond to the mechanical stimulus. The main dimensions of the flexure structure are provided in Figure 34c, which yield about 21N/cm total stiffness, but the optimization in terms of the efficiency was not done in this work.

4.3. Humidity and pressure effects on the output of TENG

4.3.1. Experimental procedure

An apparatus in Figure 35a was employed to examine the effect of the environment relative humidity (RH) and pressure on the charge amplitude. TENG was operated in the desiccator under controlled RH and pressure. The humid air from a water reservoir and the dry air from a dry air cylinder (Matheson, water content<6ppm) were fed into the desiccator through a 3-way valve. By switching the valve between the humid/dry air sources, the humidity inside the chamber could be either increased or decreased. The desiccator was connected to a vacuum pump and the pressure inside the desiccator was controlled through adjusting the pumping rate. The humidity sensor, HIH-5031 from Honeywell, can measure RH with an accuracy of ±3% from 11% to 89% and ±7% otherwise, with a specified response time of 5s. The pressure sensor was the MKS Baratron 626B with 1000 Torr range.

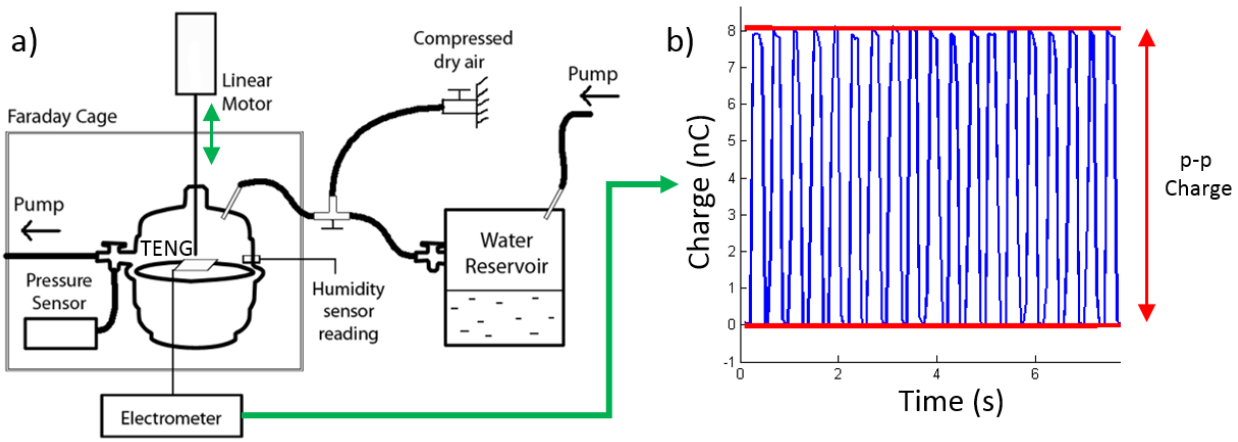

Figure 35. Experiment setup and measurement for environmental effects on TENG. (a) Experiment setup for humidity and pressure control, and (b) triboelectric charge generation when the device was cyclically pressed.

According to the study in [98], the generated charge on the PDMS surface will not be stabilized and maximized until after a few hundreds cycles. To minimize the effect of this "warm-up" process, the linear motor was kept running throughout the whole experiment, pressing and releasing the TENG at a frequency of 2.5Hz. This frequency was chosen to acquire data in a reasonable time and to maintain the mechanical stability during the experiment.

The humidity in the desiccator was increased or decreased in steps of approximately 10% between 10% and 90% by feeding different amount of the humid air and the dry air into the desiccator at about 5L/min, with negligible pressure variation. After the desired level of RH was reached, the air flow was stopped and the data was recorded, as shown in Figure 35a-b. This procedure was repeated continuously for different RH levels when RH decreased from 90% to 10% and increased from 10% back to 90%. Many cycles have been

tested and the reproducibility was confirmed. The charges from the electrodes were recorded by an electrometer (Keithley 6517B). The measured charge was smaller than the maximum charge obtained by the hand pressure due to the smaller force from the linear motor and the larger capacitance from longer leading wires. Since the linear motor was kept running all the time, the charge vs. time plot was periodic as shown in Figure 35b. All the maximum and minimum charge values in a 10s window were captured, and the peak-to-peak (p-p) values were calculated and averaged. The average p-p charge was plotted against different humidity level in Figure 36a for three cycles of decreasing and increasing RH. Additionally, to examine the transient response of p-p charge to RH, the RH was decreased or increased all the way to 10% or 90% by feeding only the dry air or humid air respectively, and the p-p amplitude of generated charges with time was recorded and shown in Figure 36c-d.

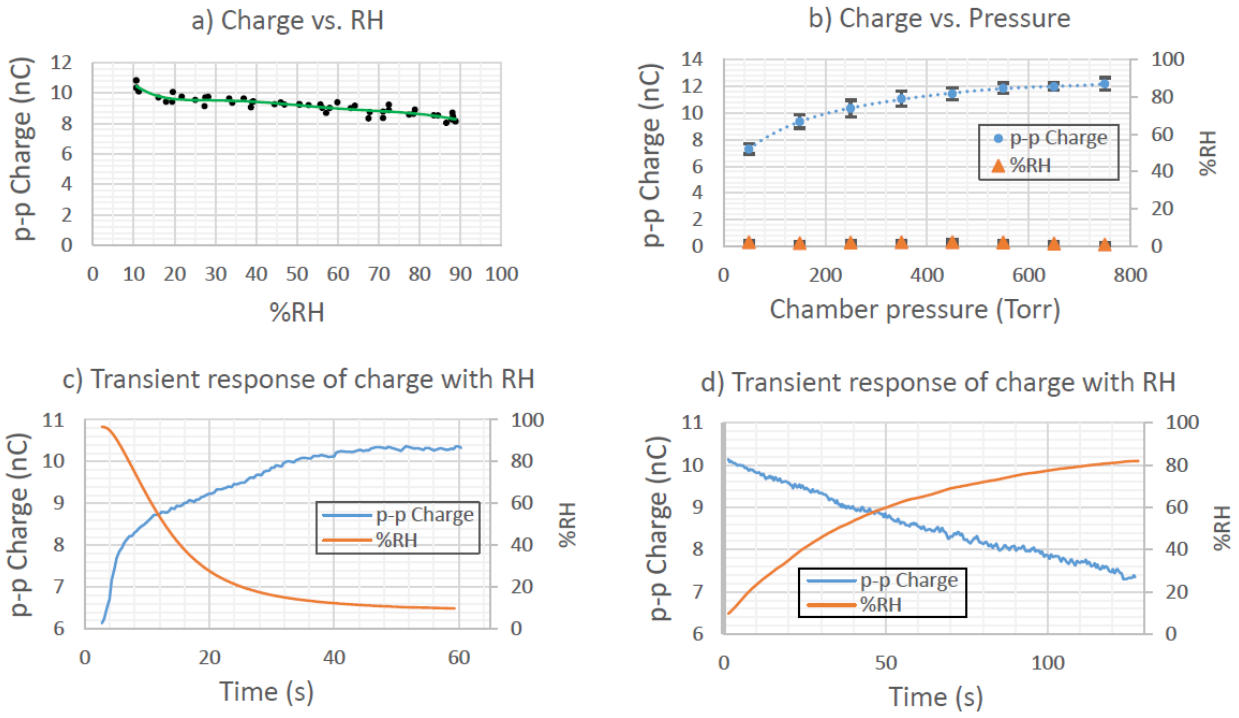

Figure 36. Humidity and pressure dependence of charge generation. (a) p-p charge at various RH with fitted trend line, (b) p-p charge at various pressure with fitted trend line, c) The response of p-p charge with time as the RH is continuously reduced from 95% to 10%, and (d) The response of p-p charge with time as the RH is continuously increased from 10% to 82% d). All results are at room temperature of 25-27°C

In the pressure dependence experiment, the chamber was pumped down from atmospheric pressure to some targeted levels at 650, 550, 450, 350, 250, 150 and 50 Torr with an error of ±8 Torr. The RH was maintained close to 0% in the experiment to minimize the effect of the pressure on the RH change. Similar to the humidity experiment, the linear motor was also kept running throughout the experiment at 2.5 Hz. This pressure test was repeated three times and the results were averaged and summarized in Figure 36b with the error bar showing one standard deviation of the data.

4.3.2. Humidity dependence of TENG charge output

As shown in Figure 36a, the p-p charge increases about 25% when RH decreases from 90% to 10%, and the p-p charge decreases to its original level when the RH increases back to 90% from 10%. RH reading produces a larger error outside 10%-90% range, but similar trend has been observed, i.e. generated charges increase when the RH decreases. The trend found in this experiment suggests that in ambient condition, high humidity is not favorable for triboelectric effect between PDMS and aluminum. The effect of the humidity on other materials needs further investigation.

The adsorbed water layer plays an important role in the charge generation [95]. Although the water layer is necessary to distribute and separate the charge, the required layer should be thin for ion transfer mechanism, probably below 2nm. A thick water layer will increase the surface conductivity, and therefore, will discharge the surfaces. Measurements of the average thickness of the adsorbed water layer have also been performed for materials with various compositions, showing different values for different compositions [93]. Thus, this experiment suggests that at ambient condition, the water adsorbed on the surfaces from the high RH dissipates the generated charge and is not in favor of TENG.

The transient result is shown in Figure 36c and 36d. It should be noted that the sharp increase at the early stage in Figure 36c is due to the fact that reducing RH is faster than increasing RH in this experiment setup. The results show that the p-p charge responds instantaneously to the change of RH, and its value at each RH agrees well with the values

obtained in Figure 36a (when the RH is varied step by step). The finite response time of the RH sensor does not appear to significantly affect these transient data, possibly because the change in RH happens in an extended time.

4.3.3. Pressure dependence of TENG charge output

According to Figure 36b, the p-p charge decreases with increasing rate as the pressure decreases from ambient pressure to 50 Torr. Because lowering the chamber pressure will cause the adsorbed water layer to evaporate, the result suggests that decreasing adsorbed water no longer favors the triboelectric charging. Combining with the results from humidity experiment, an optimal amount of adsorbed water appears to be at about atmospheric pressure and 0% RH. Since triboelectric effect usually involves different mechanisms, the charge will probably not go to zero as the pressure is further decreased. It is worth questioning how pressure would affect the charge if RH is at higher level. Although it is difficult to control RH at high values due to pressure-induced RH change, it is observed that charge starts to drop at a lower pressure than ambient pressure- at 500 Torr at 55% RH, for example. The charge actually increases slightly as the pressure is decreased slightly below the atmospheric pressure. In the other words, the optimal working condition of the TENG shifts to a lower pressure than the atmospheric pressure when the humidity is high, and the mechanism is still under further investigation. The described experiments have confirmed the ability of TENG to function at low pressure environment. They also suggest that the pressure inside the package of the TENG can also be utilized to maximize its performance.

4.4. Chapter summary

This chapter has experimentally studied the effect of the relative humidity and the pressure on the performance of TENG. TENG can work at different pressure from 50 Torr to an atmospheric pressure and at different relative humidity from 10% to 90%. This study also suggested that ambient pressure at RH close to 0% would maximize the triboelectric charge generation, and optimal pressure drops to a pressure lower than the atmospheric pressure when humidity is higher. This work explains how the surrounding conditions affect the triboelectric nanogenerator and may guide the fabrication and package of the device for the optimal performance.

CHAPTER 5. HYBRID NANOGENERATOR

5.1. Overview of the hybridization of PENG and TENG

Although the nanogenerator (NG) fabricated from FF peptide showed significant improvement in performance compared to other bio-inspired materials, new techniques to enhance the output are needed to expand its applications. Due to their complementary effects in mechanical energy harvesting, piezoelectric nanogenerators (PENG) have been proposed to be hybridized with triboelectric nanogenerators (TENG) [102-105]. While PENG converts deformation of the piezoelectric material into electricity, TENG converts relative motion into electricity through contact electrification and electrostatic induction [27]. The available ambient mechanical energy can be provided to the NG in two forms, i.e. relative motion and material deformation, so it is advantageous to combine TENG and PENG.

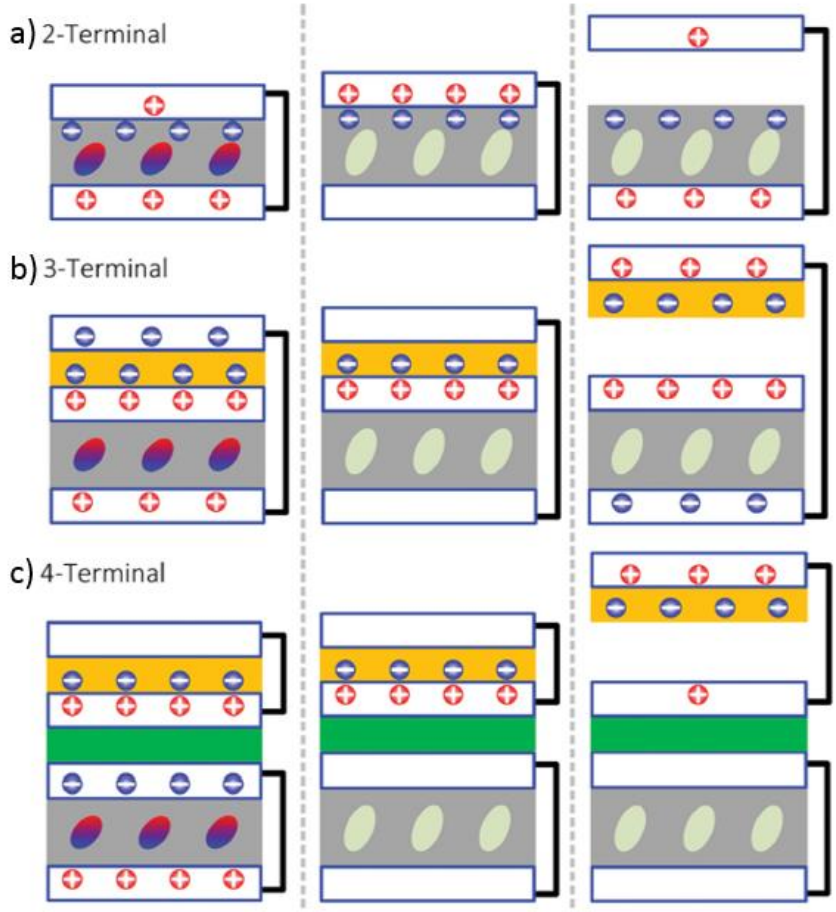

Figure 37. Charge generated at contact-press state, contact-release state and separate-release state for the three typical types of hybrid PENG-TENG [103].

Depending on the number of wire terminals, hybrid PENG-TENG can be divided into three typical structures: 2-terminal, 3-terminal and 4-terminal, as shown in Figure 37 [103]. The 2-terminal type can be achieved by utilizing the piezoelectric material also as a triboelectric material as in Figure 37a, and a real device has been demonstrated using PVDF [104]. Connecting the PENG in series with the TENG gives the 3-terminal configuration, as in Figure 37b, while simple stacking with the two NGs working independently as in

Figure 37c gives the 4-terminal configuration. Among them, the 3-terminal type is often employed by simply utilizing the metal electrode of PENG as a contact material for TENG, and an example of r-shaped design is shown in Figure 38.

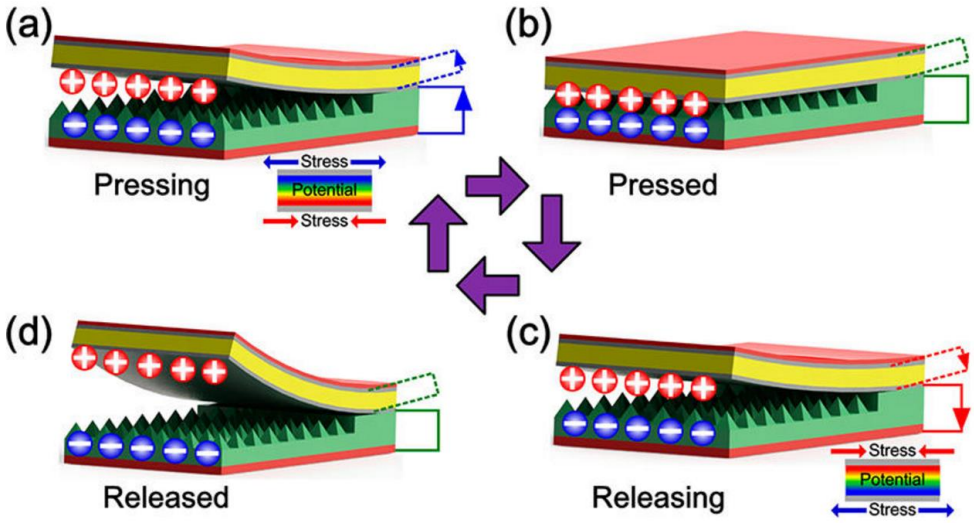

Figure 38. An r-shaped hybrid NG which utilizes one metal electrode of a thin film PENG as the contact material for TENG [105].

A disadvantage of 3-or-more-terminal NG is that the NG would require more space for its operation and higher complexity in fabrication. Utilizing piezoelectric material as the triboelectric material to achieve 2-terminal would significantly restrict the material choices, and the device still requires an internal gap for the TENG to operate. In this Chapter the single-electrode TENG is proposed to be used with FF peptide PENG to achieve 2-terminal configuration and reduce the required number of layers in TENG while still enhancing the overall output.

5.2. Single-electrode TENG integrated with FF peptide PENG and the energy conversion process

The schematic and photo of the hybrid NG are shown in Figure 39a and 39b. The FF microrod array was fabricated using the epitaxial growth process described in Chapter 3. Accordingly, The FF-based PENG was built by sandwiching the FF microrods array between two 1.25x1.25 cm^2 gold-coated silicon substrate. The TENG materials selected in this study were polyethylene terephthalate (PET) (purchased from McMaster) and Kapton (purchased from DuPont) due to their stable output and distinct charge affinity. The single-electrode TENG was assembled by laminating a pristine PET film on the top electrode of the PENG, while the ground is connected to the bottom electrode of the PENG, as shown in Figure 39a. Thus effectively no additional conductive electrodes needed to be fabricated for the single-electrode TENG because it utilized the already available ones of the PENG, simplifying the configuration of the hybrid NG. The PENG, together with the lower part of the TENG, were mounted on the bottom of a plastic enclosure. The top part of the single-electrode TENG, which is standalone pristine Kapton film with no wire connection, was attached to the movable top part of the enclosure to form a compact setup for characterization.

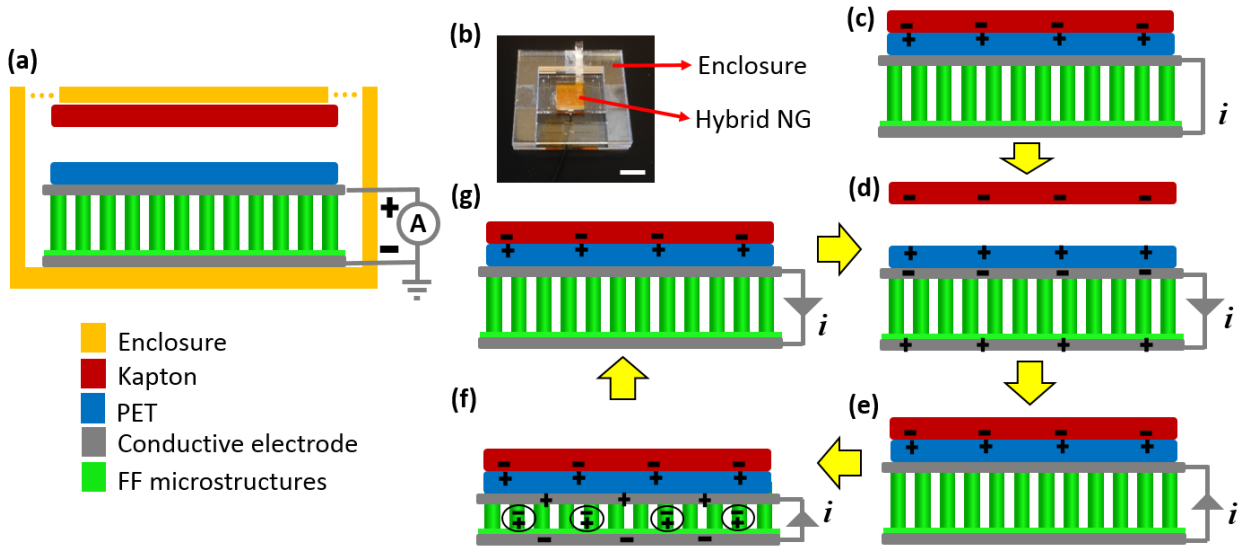

Figure 39. Hybrid NG structure and working mechanism. (a) Schematic of the structure of the hybrid NG and the polarity of the measurement connection. (b) Photograph of the real hybrid NG with a compact acrylic enclosure. Scale bar is 1cm. (c)-(g) Energy conversion process of the hybrid NG.

The energy conversion process is explained in Figure 39c-g. Because Kapton and PET have different charge affinity, upon contact Kapton gains negative charge and PET gains positive charge [25, 27], Figure 39c. When the two surfaces first separate, current flows from the top to the bottom electrode to balance the charge (Figure 39d). This current is positive according to the connection of the measuring device. As Kapton moves back to contact but with no pressing force, current flows from the bottom to the top electrode (Figure 39e), and is therefore negative. As the linear actuator continues to apply pressing force to the NG, the Kapton film side compresses the piezoelectric FF microrods and current continues to flow to the top electrode due to the electrical dipole created in the piezoelectric FF microrod under pressure. When the pressing force is released, the FF

microrods are no longer compressed and the current flows back to the bottom electrode (Figure 39g). The Kapton film is then separated from the PET, as in Figure 39d and current continues to flow back to the bottom electrode to complete one cycle. As a result, the hybrid device can harvest energy from both significant movement of the top layer of the TENG and minute deformation in piezoelectric materials caused by the pressing force.

5.3. Output characterization of the hybrid nanogenerator

Measurements were conducted for the piezoelectric and triboelectric output separately in Figure 40 to discern the constructive output in the subsequent hybrid NG. The independent piezoelectric output was obtained by keeping the Kapton film side pressing on the PET side with a force larger than zero, which prevented the separation of the two layers of the TENG. This process is represented by the states in Figure 39f and 39g. The triboelectric output was independently obtained by moving the Kapton film to just in

contact with the PET film with insignificant pressing force and then separating them. This process is similar to the states in Figure 39d and Figure 39e.

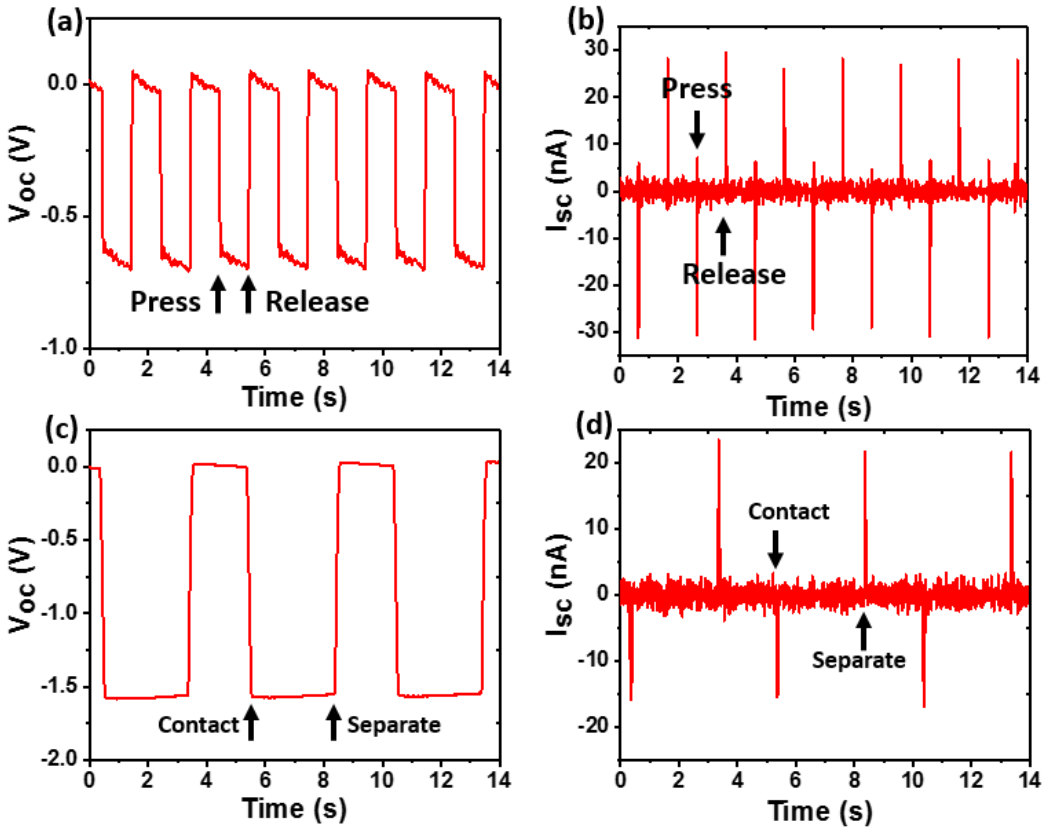

Figure 40. Output of PENG and TENG when working separately. Open-circuit voltage and short-circuit current of FF PENG only (a)-(b), which involved only cyclic pressing force without relative motion and TENG only (c)-(d), which involved only cyclic motion without pressing force.

According to Figure 40a-b, the V_{oc} and I_{sc} from the piezoelectric nanogenerator were about 0.7 V and 30 nA, respectively, under an applied force of 50 N. The average charge, calculated by the area under the current peak, was 406 pC. These results were consistent with the reported output of FF-based NG [62]. According to figure 40c-d, the

V_{oc} and I_{sc} from the triboelectric nanogenerator were about 1.6 V and 20 nA, respectively, with the average charge of 875 pC. The lower peak current but higher charge of the TENG part was due to the relatively slow motion of the Kapton film to reduce the impact on the FF microrod array upon contact. The current direction and voltage polarity of triboelectric output were in the same direction as the piezoelectric output. Two outputs were thus expected to be superimposed constructively as both contact and pressing are performed.

The piezoelectric and triboelectric power generation processes were then combined to demonstrate the enhancement of the FF-based NG. A 4-step force profile shown in Figure 41a was applied to the hybrid NG to provide a press/release cycle after the contact between the Kapton and PET surfaces. The initial force was about 10 N, which was determined experimentally to be just enough to resist the spring force to keep the Kapton and PET films in contact, while not producing significant pressure on the piezoelectric FF microrod array. Then an additional 50 N force was applied to the FF PENG to deform the piezoelectric FF microrods, with a total applied force of 60N. The pressing force was then released, but the contact between the Kapton and the PET film was still maintained. Finally, the polymer films were separated as no force was applied. The output open-circuit voltage and short-circuit current were recorded during the force application process as shown in Figure 41b and 41c.

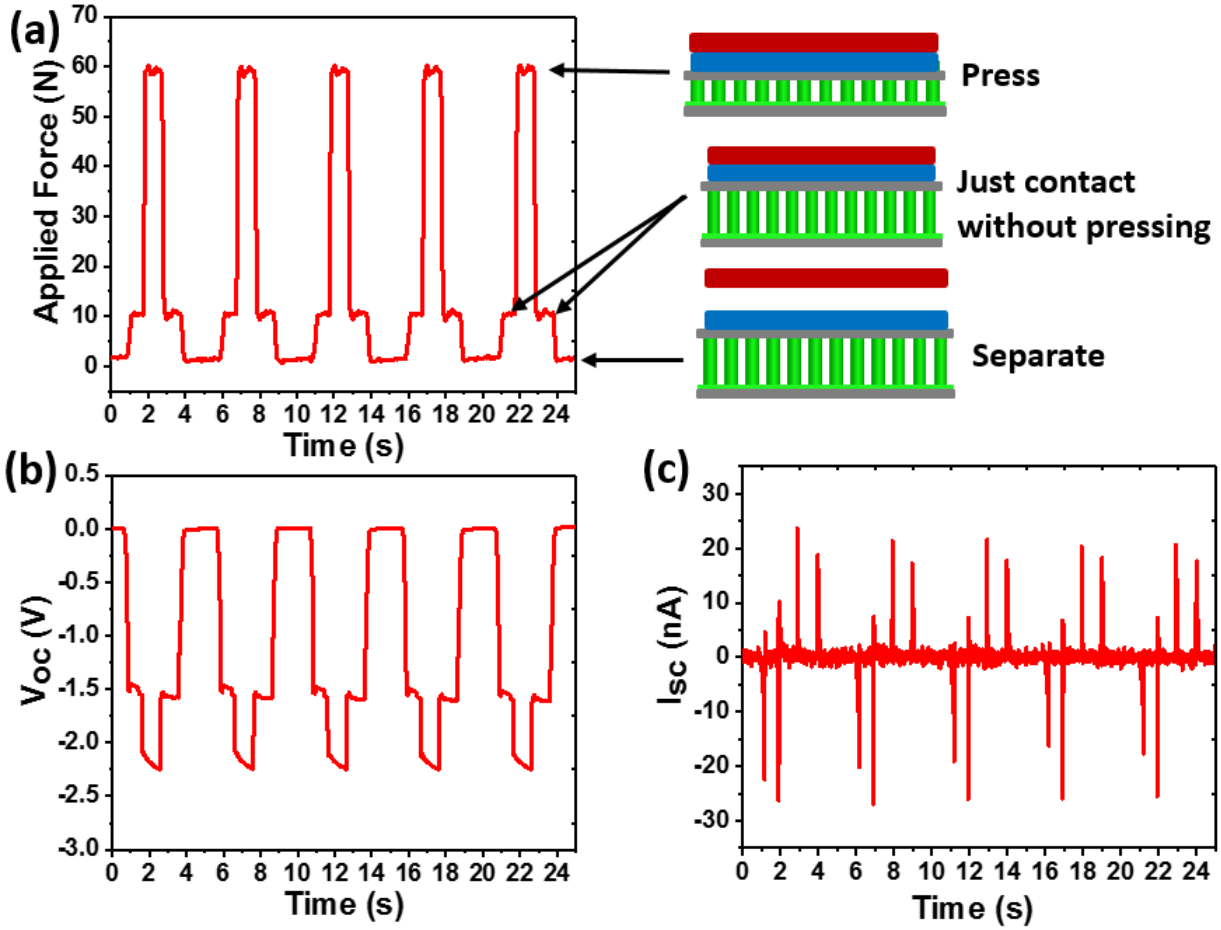

Figure 41. Output of the hybridized NG. (a) Profile of the applied force on the hybrid NG and the corresponding state of the hybrid NG at each force level. (b),-(c) Open-circuit voltage and short-circuit current of the hybrid NG under the force profile in (a).

Figure 41b shows a constructive step as the FF-based PENG is pressed, with total output voltage up to 2.2 V compared to 0.7 V or 1.6 V if only either PENG or TENG operates, respectively. The voltage output has a rectangular waveform instead of peaks because the insulating property of FF crystals as well as the high internal resistance of the measuring electrometer prevented the unintentional discharge. Figure 41c shows four

current peaks in one force application cycle which are also in the constructive direction as the force is applied or withdrawn. The directions of the output current were consistent with the process explained in Figure 39d-g, verifying the constructive energy conversion mechanism of the hybrid NG.

5.4. Chapter summary

In conclusion, we have demonstrated a hybrid NG structure that utilized single-electrode TENG to provide constructive additional voltage and current output to the FF-based PENG. The design of our hybrid NG was simple because the addition of single-electrode TENG to the existing FF-based PENG did not require additional conductive electrodes. Although Kapton and PET were selected in this study, the TENG materials can still be optimized to best suit a specific application. Since the Kapton film was not connected to the circuit, it could be designed to be part of the environment of the hybrid NG, which could simplify the fabrication process and reduce the dimension of the hybrid NG. Our study can serve as a guideline for the design of future FF-based device as well as future hybridization between PENG and TENG.

CHAPTER 6. CONCLUSIONS

FF peptide has the potential to become one of the most technologically important bioinspired piezoelectric materials for small-scale energy conversion thanks to its strong piezoelectricity and its inherent biological properties. This thesis has achieved advances in the development of FF peptide towards nanogenerator application.

First, in Chapter 2, a low temperature epitaxial growth process has been developed to obtain vertically aligned FF peptide microrod arrays. The vertical alignment of the array is achieved by engineering the amorphous layer of FF into a seed layer with a preferential vertical orientation. The circulation of moist air and the thickness of the amorphous layer is found to control the amount of vertical domain in the seed. By putting the seed layer in a water solution saturated with FF peptide and letting the water evaporates in room temperature, the outgrowth of vertical microrods from the seed over the entire substrate is observed due to supersaturation. Examination of the morphology and crystal structure of the obtained microrods as well as the original seed layer confirms they have hexagonal symmetry which lacks an inversion center. Effective piezoelectric coefficient d_{33} is also measured for both seed and microrods, which yield a value of up to 9.9 pm/V.

Although structurally vertical alignment is achieved, opposite polarizations in adjacent microrods are observed and the overall piezoelectric effect of the array is reduced. The unswitchability of FF polarization makes it practically impossible to pole the FF array by an applied electric field after the growth has completed. Chapter 3 addresses this problem by applying an electric field during the epitaxial growth, and uniform polarization

in opposite directions has been achieved. The effective piezoelectric coefficient d_{33} is measured to be up to 17.9 pm/V. Moreover, the elevated temperature at 55^{o}C is also found to facilitate longer and more uniform microrods. The improved microrod array is then used to fabricate an FF peptide PENG which shows better performance compared to other bioinspired materials or even some inorganic materials.

TENG has recently emerged as a nanogenerator technology to harvest mechanical energy from large motion, as opposed to harvesting energy from tiny deformation in PENG. Thus, hybridizing TENG with PENG can enhance the outputs of just the PENG alone. To facilitate future integration of the two types of nanogenerators, Chapter 4 investigates the performance of TENG under various environmental conditions such as RH and pressure. The effects of RH and pressure have been found to closely relate to the adsorbed water layer on the contacting surfaces. The results can serve as a guideline to the design of TENG for different conditions.

Finally, Chapter 5 explores a new structure to hybridize FF peptide PENG with single-electrode TENG. The outputs of the two nanogenerators are successfully combined constructively. The hybrid energy conversion process is explained and verified by experimental data. Moreover, the use of single-electrode TENG on top of the PENG enables hybridization without the need of additional electrodes, and thus the dimensions and complexity of the fabrication process can be potentially reduced.

References

1. Wang, Z.L., *Self-Powered Nanosensors and Nanosystems.* Advanced Materials, 2012. **24**(2): p. 280-285.
2. Fukada, E. and I. Yasuda, *On the piezoelectric effect of bone.* Journal of the physical society of Japan, 1957. **12**(10): p. 1158-1162.
3. Halperin, C., et al., *Piezoelectric effect in human bones studied in nanometer scale.* Nano Letters, 2004. **4**(7): p. 1253-1256.
4. Marino, A.A. and R.O. Becker, *Piezoelectric effect and growth control in bone.* 1970.
5. Duarte, L., *The stimulation of bone growth by ultrasound.* Archives of Orthopaedic and Trauma Surgery, 1983. **101**(3): p. 153-159.
6. Patel, N. and M.-M. Poo, *Orientation of neurite growth by extracellular electric fields.* Journal of Neuroscience, 1982. **2**(4): p. 483-496.
7. Zhao, M., J.V. Forrester, and C.D. McCaig, *A small, physiological electric field orients cell division.* Proceedings of the National Academy of Sciences, 1999. **96**(9): p. 4942-4946.
8. Cohen, D.J., W.J. Nelson, and M.M. Maharbiz, *Galvanotactic control of collective cell migration in epithelial monolayers.* Nature materials, 2014. **13**(4): p. 409-417.
9. Rajabi, A.H., M. Jaffe, and T.L. Arinzeh, *Piezoelectric materials for tissue regeneration: a review.* Acta biomaterialia, 2015. **24**: p. 12-23.
10. Valentini, R.F., et al., *Electrically charged polymeric substrates enhance nerve fibre outgrowth in vitro.* Biomaterials, 1992. **13**(3): p. 183-190.
11. Royo-Gascon, N., et al., *Piezoelectric substrates promote neurite growth in rat spinal cord neurons.* Annals of biomedical engineering, 2013. **41**(1): p. 112-122.
12. Ribeiro, C., et al., *Dynamic piezoelectric stimulation enhances osteogenic differentiation of human adipose stem cells.* Journal of Biomedical Materials Research Part A, 2015. **103**(6): p. 2172-2175.
13. Ghosh, S., et al., *Piezoelectric response of scleral collagen.* Journal of Biomedical Materials Research Part A, 1998. **39**(3): p. 453-457.
14. Fukada, E., *Piezoelectric properties of biological polymers.* Quarterly reviews of biophysics, 1983. **16**(01): p. 59-87.
15. Hoummady, M., A. Campitelli, and W. Wlodarski, *Acoustic wave sensors: design, sensing mechanisms and applications.* Smart materials and structures, 1997. **6**(6): p. 647.
16. Dubois, M.-A. and C. Muller, *Thin-Film Bulk Acoustic Wave Resonators*, in *MEMS-based Circuits and Systems for Wireless Communication*. 2013, Springer. p. 3-28.
17. Koike, J., K. Shimoe, and H. Ieki, *1.5 GHz low-loss surface acoustic wave filter using ZnO/sapphire substrate.* Japanese journal of applied physics, 1993. **32**(5S): p. 2337.
18. Flewitt, A., et al., *ZnO based SAW and FBAR devices for bio-sensing applications.* Journal of Non-Newtonian Fluid Mechanics, 2015. **222**: p. 209-216.

19. Länge, K., B.E. Rapp, and M. Rapp, *Surface acoustic wave biosensors: a review.* Analytical and bioanalytical chemistry, 2008. **391**(5): p. 1509-1519.
20. Rocha-Gaso, M.-I., et al., *Surface generated acoustic wave biosensors for the detection of pathogens: A review.* Sensors, 2009. **9**(7): p. 5740-5769.
21. Wang, Z.L. and J. Song, *Piezoelectric nanogenerators based on zinc oxide nanowire arrays.* Science, 2006. **312**(5771): p. 242-246.
22. Wang, X., et al., *Direct-current nanogenerator driven by ultrasonic waves.* Science, 2007. **316**(5821): p. 102-105.
23. Park, K.-I., et al., *Piezoelectric BaTiO3 thin film nanogenerator on plastic substrates.* Nano letters, 2010. **10**(12): p. 4939-4943.
24. Zeng, W., et al., *Highly durable all-fiber nanogenerator for mechanical energy harvesting.* Energy & Environmental Science, 2013. **6**(9): p. 2631-2638.
25. Fan, F.-R., Z.-Q. Tian, and Z.L. Wang, *Flexible triboelectric generator.* Nano Energy, 2012. **1**(2): p. 328-334.
26. Wang, Z.L., *Triboelectric nanogenerators as new energy technology and self-powered sensors–Principles, problems and perspectives.* Faraday Discuss., 2015. **176**: p. 447-458.
27. Wang, Z.L., *Triboelectric nanogenerators as new energy technology for self-powered systems and as active mechanical and chemical sensors.* ACS nano, 2013. **7**(11): p. 9533-9557.
28. Yang, Y., et al., *Pyroelectric nanogenerators for harvesting thermoelectric energy.* Nano letters, 2012. **12**(6): p. 2833-2838.
29. Yang, Y., et al., *Flexible Pyroelectric Nanogenerators using a Composite Structure of Lead-Free KNbO3 Nanowires.* Advanced Materials, 2012. **24**(39): p. 5357-5362.
30. Yang, Y., et al., *Nanowire-composite based flexible thermoelectric nanogenerators and self-powered temperature sensors.* Nano Research, 2012: p. 1-8.
31. Yang, Y., et al., *Thermoelectric nanogenerators based on single Sb-doped ZnO micro/nanobelts.* ACS nano, 2012. **6**(8): p. 6984-6989.
32. Yang, R., et al., *Power generation with laterally packaged piezoelectric fine wires.* Nature nanotechnology, 2009. **4**(1): p. 34-39.
33. Zhu, G., et al., *Flexible high-output nanogenerator based on lateral ZnO nanowire array.* Nano letters, 2010. **10**(8): p. 3151-3155.
34. Xu, S., et al., *Self-powered nanowire devices.* Nature nanotechnology, 2010. **5**(5): p. 366-373.
35. Diaz, A. and R. Felix-Navarro, *A semi-quantitative tribo-electric series for polymeric materials: the influence of chemical structure and properties.* Journal of Electrostatics, 2004. **62**(4): p. 277-290.
36. Wang, Z.L., *Zinc oxide nanostructures: growth, properties and applications.* Journal of Physics: Condensed Matter, 2004. **16**(25): p. R829.
37. Pan, Z.W., Z.R. Dai, and Z.L. Wang, *Nanobelts of semiconducting oxides.* Science, 2001. **291**(5510): p. 1947-1949.

38. Zhu, R., et al., *Uniform zinc oxide nanowire arrays grown on nonepitaxial surface with general orientation control.* Nano letters, 2013. **13**(11): p. 5171-5176.
39. Qi, Y., et al., *Piezoelectric ribbons printed onto rubber for flexible energy conversion.* Nano letters, 2010. **10**(2): p. 524-528.
40. Nguyen, T.D., et al., *Piezoelectric nanoribbons for monitoring cellular deformations.* Nature nanotechnology, 2012. **7**(9): p. 587-593.
41. Koka, A. and H.A. Sodano, *High-sensitivity accelerometer composed of ultra-long vertically aligned barium titanate nanowire arrays.* Nature communications, 2013. **4**.
42. Chang, C., et al., *Direct-write piezoelectric polymeric nanogenerator with high energy conversion efficiency.* Nano letters, 2010. **10**(2): p. 726-731.
43. Lee, B.Y., et al., *Virus-based piezoelectric energy generation.* Nature nanotechnology, 2012. **7**(6): p. 351-356.
44. Shin, D.-M., et al., *Bioinspired piezoelectric nanogenerators based on vertically aligned phage nanopillars.* Energy & Environmental Science, 2015. **8**(11): p. 3198-3203.
45. Rodriguez, B.J., et al., *Electromechanical imaging of biomaterials by scanning probe microscopy.* Journal of structural biology, 2006. **153**(2): p. 151-159.
46. Ghadiri, M.R., et al., *Self-assembling organic nanotubes based on a cyclic peptide architecture.* Nature, 1993. **366**(6453): p. 324.
47. Hartgerink, J.D., E. Beniash, and S.I. Stupp, *Self-assembly and mineralization of peptide-amphiphile nanofibers.* Science, 2001. **294**(5547): p. 1684-1688.
48. Vauthey, S., et al., *Molecular self-assembly of surfactant-like peptides to form nanotubes and nanovesicles.* Proceedings of the National Academy of Sciences, 2002. **99**(8): p. 5355-5360.
49. Reches, M. and E. Gazit, *Casting metal nanowires within discrete self-assembled peptide nanotubes.* Science, 2003. **300**(5619): p. 625-627.
50. Kholkin, A., et al., *Strong piezoelectricity in bioinspired peptide nanotubes.* Acs Nano, 2010. **4**(2): p. 610-614.
51. Kol, N., et al., *Self-assembled peptide nanotubes are uniquely rigid bioinspired supramolecular structures.* Nano letters, 2005. **5**(7): p. 1343-1346.
52. Niu, L., et al., *Using the bending beam model to estimate the elasticity of diphenylalanine nanotubes.* Langmuir, 2007. **23**(14): p. 7443-7446.
53. Santhanamoorthi, N., et al., *Diphenylalanine peptide nanotube: charge transport, band gap and its relevance to potential biomedical applications.* Adv. Mater. Lett, 2011. **2**: p. 100.
54. Silva, R.F., et al., *L-diphenylalanine microtubes as a potential drug-delivery system: characterization, release kinetics, and cytotoxicity.* Langmuir, 2013. **29**(32): p. 10205-10212.
55. Yan, X., P. Zhu, and J. Li, *Self-assembly and application of diphenylalanine-based nanostructures.* Chemical Society Reviews, 2010. **39**(6): p. 1877-1890.
56. Görbitz, C.H., *Nanotube formation by hydrophobic dipeptides.* Chemistry–A European Journal, 2001. **7**(23): p. 5153-5159.

57. Görbitz, C.H., *The structure of nanotubes formed by diphenylalanine, the core recognition motif of Alzheimer's β-amyloid polypeptide.* Chemical communications, 2006(22): p. 2332-2334.
58. Wang, M., et al., *Charged diphenylalanine nanotubes and controlled hierarchical self-assembly.* Acs Nano, 2011. **5**(6): p. 4448-4454.
59. Gan, Z., et al., *Light-Induced Ferroelectricity in Bioinspired Self-Assembled Diphenylalanine Nanotubes/Microtubes.* Angewandte Chemie International Edition, 2013. **52**(7): p. 2055-2059.
60. Heredia, A., et al., *Temperature-driven phase transformation in self-assembled diphenylalanine peptide nanotubes.* Journal of Physics D: Applied Physics, 2010. **43**(46): p. 462001.
61. Nguyen, V., K. Jenkins, and R. Yang, *Epitaxial growth of vertically aligned piezoelectric diphenylalanine peptide microrods with uniform polarization.* Nano Energy, 2015. **17**: p. 323-329.
62. Nguyen, V., et al., *Self-assembly of diphenylalanine peptide with controlled polarization for power generation.* Nature Communications, 2016. **7**: p. 13566.
63. Nguyen, V. and R. Yang, *Effect of humidity and pressure on the triboelectric nanogenerator.* Nano Energy, 2013. **2**(5): p. 604-608.
64. Adler-Abramovich, L., et al., *Self-assembled arrays of peptide nanotubes by vapour deposition.* Nature nanotechnology, 2009. **4**(12): p. 849-854.
65. Ryu, J. and C.B. Park, *High-Temperature Self-Assembly of Peptides into Vertically Well-Aligned Nanowires by Aniline Vapor.* Advanced Materials, 2008. **20**(19): p. 3754-3758.
66. Beker, P. and G. Rosenman, *Bioinspired nanostructural peptide materials for supercapacitor electrodes.* Journal of Materials Research, 2010. **25**(08): p. 1661-1666.
67. Ryu, J. and C.B. Park, *Synthesis of Diphenylalanine/Polyaniline Core/Shell Conducting Nanowires by Peptide Self-Assembly.* Angewandte Chemie International Edition, 2009. **48**(26): p. 4820-4823.
68. Ryu, J., et al., *Synthesis of diphenylalanine/cobalt oxide hybrid nanowires and their application to energy storage.* 2010.
69. Ryu, J. and C.B. Park, *Solid-phase growth of nanostructures from amorphous peptide thin film: effect of water activity and temperature.* Chemistry of Materials, 2008. **20**(13): p. 4284-4290.
70. Ryu, J. and C.B. Park, *High stability of self-assembled peptide nanowires against thermal, chemical, and proteolytic attacks.* Biotechnology and bioengineering, 2010. **105**(2): p. 221-230.
71. Reches, M. and E. Gazit, *Controlled patterning of aligned self-assembled peptide nanotubes.* Nature nanotechnology, 2006. **1**(3): p. 195-200.
72. Huang, R., et al., *Hierarchical, interface-induced self-assembly of diphenylalanine: formation of peptide nanofibers and microvesicles.* Nanotechnology, 2011. **22**(24): p. 245609.
73. Kim, J., et al., *Role of water in directing diphenylalanine assembly into nanotubes and nanowires.* Advanced Materials, 2010. **22**(5): p. 583-587.

74. Adler-Abramovich, L., et al., *Thermal and chemical stability of diphenylalanine peptide nanotubes: implications for nanotechnological applications.* Langmuir, 2006. **22**(3): p. 1313-1320.
75. Mason, T.O., et al., *Expanding the solvent chemical space for self-assembly of dipeptide nanostructures.* ACS nano, 2014. **8**(2): p. 1243-1253.
76. Yan, X., J. Li, and H. Möhwald, *Self-Assembly of Hexagonal Peptide Microtubes and Their Optical Waveguiding.* Advanced Materials, 2011. **23**(25): p. 2796-2801.
77. Sakurai, M., P. Koley, and M. Aono, *A new approach to molecular self-assembly through formation of dipeptide-based unique architectures by artificial supersaturation.* Chemical Communications, 2014. **50**(83): p. 12556-12559.
78. Su, Y., et al., *A peony-flower-like hierarchical mesocrystal formed by diphenylalanine.* Journal of Materials Chemistry, 2010. **20**(32): p. 6734-6740.
79. Li, Q., et al., *Controlled rod nanostructured assembly of diphenylalanine and their optical waveguide properties.* ACS nano, 2015. **9**(3): p. 2689-2695.
80. Zhang, J., et al., *Unidirectionally aligned diphenylalanine nanotube/microtube arrays with excellent supercapacitive performance.* Nano Research, 2014. **7**(6): p. 929-937.
81. Görbitz, C.H., *Microporous organic materials from hydrophobic dipeptides.* Chemistry–A European Journal, 2007. **13**(4): p. 1022-1031.
82. Zhang, S., *Fabrication of novel biomaterials through molecular self-assembly.* Nature biotechnology, 2003. **21**(10): p. 1171-1178.
83. Mata, A., et al., *Micropatterning of bioactive self-assembling gels.* Soft Matter, 2009. **5**(6): p. 1228-1236.
84. Ryan, K., et al., *Nanoscale piezoelectric properties of self-assembled fmoc–FF peptide fibrous networks.* ACS applied materials & interfaces, 2015. **7**(23): p. 12702-12707.
85. Bdikin, I., et al., *Polarization switching and patterning in self-assembled peptide tubular structures.* Journal of Applied Physics, 2012. **111**(7): p. 074104.
86. Bosne, E., et al., *Piezoelectric resonators based on self-assembled diphenylalanine microtubes.* Applied Physics Letters, 2013. **102**(7): p. 073504.
87. Kelly, C.M., et al., *Conformational dynamics and aggregation behavior of piezoelectric diphenylalanine peptides in an external electric field.* Biophysical chemistry, 2015. **196**: p. 16-24.
88. Wang, M., et al., *Effects of water molecules on photoluminescence from hierarchical peptide nanotubes and water probing capability.* small, 2011. **7**(19): p. 2801-2807.
89. Castillo, J., et al., *Manipulation of self-assembly amyloid peptide nanotubes by dielectrophoresis.* Electrophoresis, 2008. **29**(24): p. 5026-5032.
90. Qi, Y. and M.C. McAlpine, *Nanotechnology-enabled flexible and biocompatible energy harvesting.* Energy & Environmental Science, 2010. **3**(9): p. 1275-1285.
91. Hillenbrand, J. and G. Sessler, *Piezoelectricity in cellular electret films.* IEEE Transactions on Dielectrics and Electrical Insulation, 2000. **7**(4): p. 537-542.

92. Fan, F.-R., et al., *Transparent triboelectric nanogenerators and self-powered pressure sensors based on micropatterned plastic films.* Nano letters, 2012. **12**(6): p. 3109-3114.
93. Pence, S., V. Novotny, and A. Diaz, *Effect of surface moisture on contact charge of polymers containing ions.* Langmuir, 1994. **10**(2): p. 592-596.
94. Wiles, J.A., et al., *Effects of surface modification and moisture on the rates of charge transfer between metals and organic materials.* The Journal of Physical Chemistry B, 2004. **108**(52): p. 20296-20302.
95. McCarty, L.S. and G.M. Whitesides, *Electrostatic charging due to separation of ions at interfaces: contact electrification of ionic electrets.* Angewandte Chemie International Edition, 2008. **47**(12): p. 2188-2207.
96. Davies, D., *Charge generation on dielectric surfaces.* Journal of Physics D: Applied Physics, 1969. **2**(11): p. 1533.
97. Hogue, M., et al., *Insulator–insulator contact charging and its relationship to atmospheric pressure.* Journal of electrostatics, 2004. **61**(3): p. 259-268.
98. Zhu, G., et al., *Triboelectric-generator-driven pulse electrodeposition for micropatterning.* Nano letters, 2012. **12**(9): p. 4960-4965.
99. Wang, S., L. Lin, and Z.L. Wang, *Nanoscale triboelectric-effect-enabled energy conversion for sustainably powering portable electronics.* Nano letters, 2012. **12**(12): p. 6339-6346.
100. Zhu, G., et al., *Toward large-scale energy harvesting by a nanoparticle-enhanced triboelectric nanogenerator.* Nano letters, 2013. **13**(2): p. 847-853.
101. Zhang, X.-S., et al., *Frequency-multiplication high-output triboelectric nanogenerator for sustainably powering biomedical microsystems.* Nano letters, 2013. **13**(3): p. 1168-1172.
102. Jung, W.-S., et al., *High output piezo/triboelectric hybrid generator.* Scientific reports, 2015. **5**: p. 9309.
103. Han, M., et al., *Coupling of piezoelectric and triboelectric effects: From theoretical analysis to experimental verification.* Advanced Electronic Materials, 2015. **1**(10).
104. Bai, P., et al., *Dipole-moment-induced effect on contact electrification for triboelectric nanogenerators.* Nano Research, 2014. **7**(7): p. 990-997.
105. Han, M., et al., *r-Shaped hybrid nanogenerator with enhanced piezoelectricity.* ACS nano, 2013. **7**(10): p. 8554-8560.
106. Nguyen, V., et al., Piezoelectric peptide-based nanogenerator enhanced by single-electrode triboelectric nanogenerator. APL Materials, 2017 (accepted).

Appendix

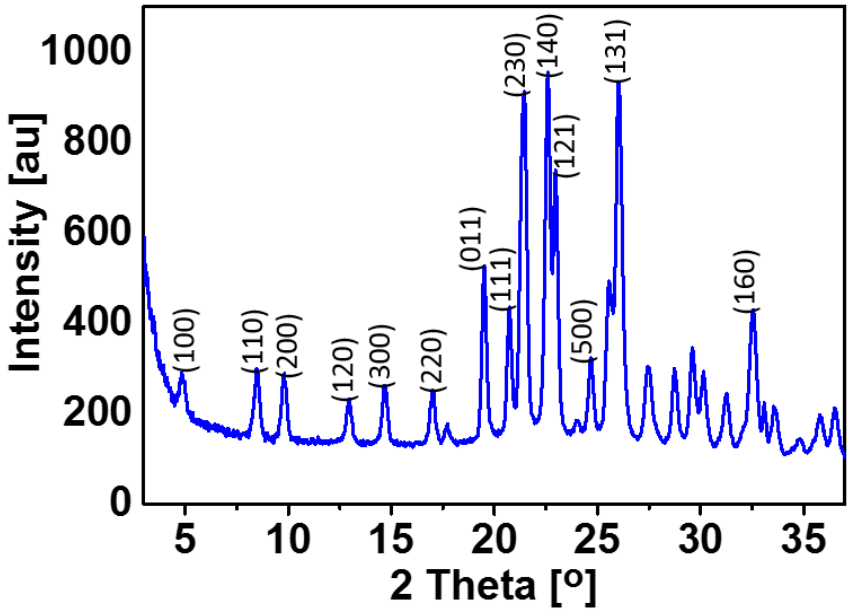

Figure A 1. XRD confirmation for the FF peptide microrod arrays grown in Chapter 3. The obtained spectrum confirms the hexagonal crystal structure with the space group $P6_1$ (noncentrosymmetric), allowing for a strong piezoelectric effect. Measurement was made using Bruker D8 system with Cobalt anode (λ=1.78899Å)

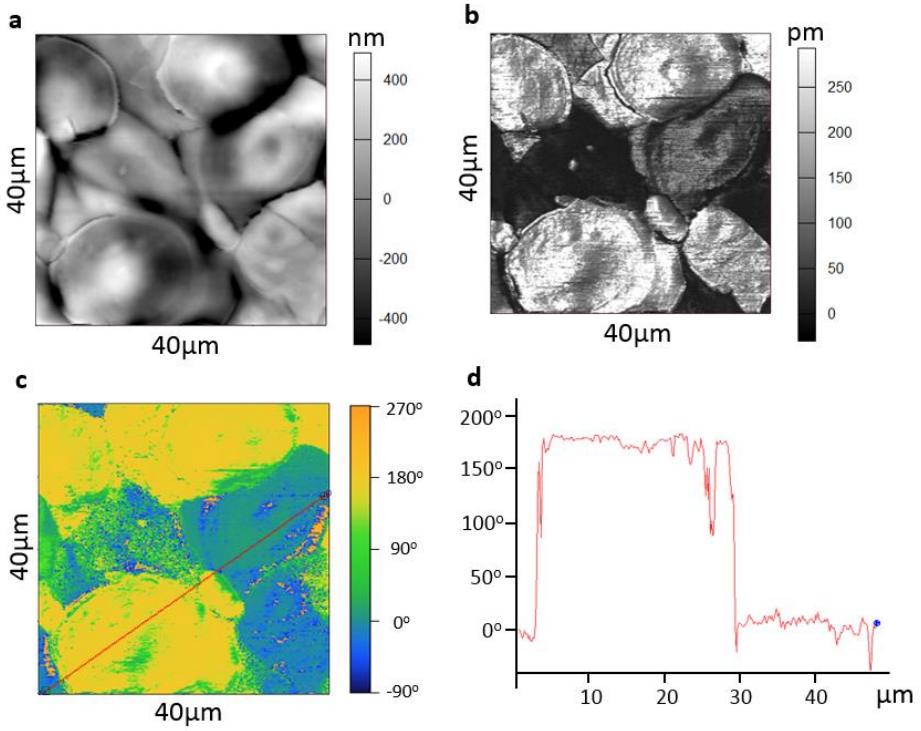

Figure A 2. PFM phase measurements of FF peptide crystals. ***FF peptide crystals in a seed layer grown with no electric field, showing both positive and negative polarities with 180^o phase difference. Topography (a), amplitude (b) and phase response (c) of FF peptide crystals with opposite polarities. (d), cross section at the red line in the phase map in (c), showing that the two polarities are approximately 180^o apart.***

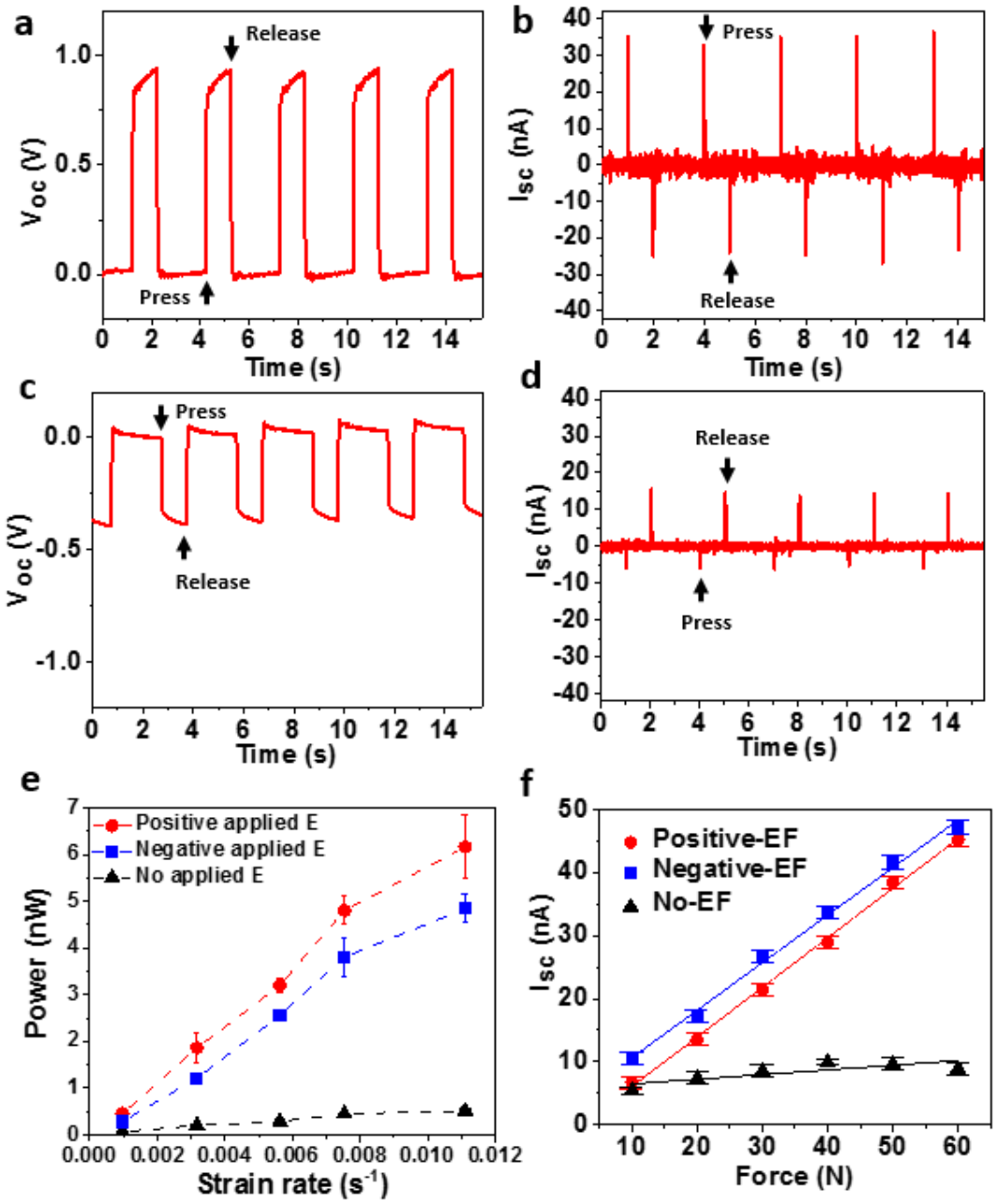

Figure A 3. Characterization of the FF peptide-based power generators. (a-d) open-circuit voltage (a,c) and short-circuit current (b,d) of generators using microrods from negative-EF growth (a,b) and no-EF growth (c,d). (e), dependence of peak output power on strain rate at 50 N applied force. The peak strain of 4.5×10^{-4} *was estimated using a*

microrod array with 34,000 rods cm^{-2}, 15 µm-diameter, 50 µm-length, and 19 GPa Young's Modulus for each rod, and the strain was reached in a time that was equal to the force rise time (460, 140, 79, 59, 40 ms). (f) dependence of peak short-circuit current on applied force.

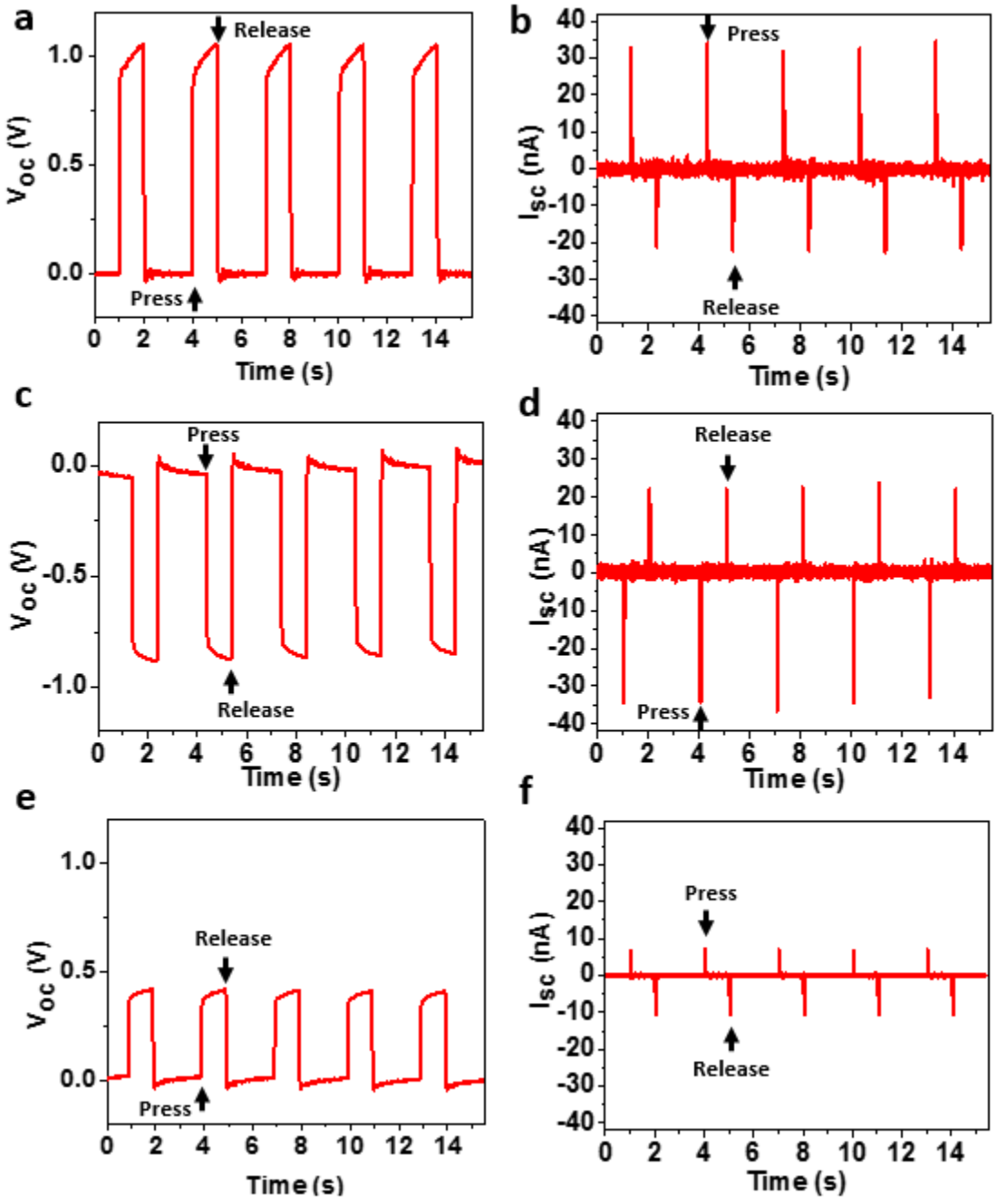

Figure A 4. Reversed connection test for FF peptide-based power generators. (a-f) open-circuit voltage (a,c,e) and short-circuit current (b,d,f) from power generators using

microrods from positive-EF growth (a,b), negative-EF growth (c,d), and no-EF growth (e,f) under reversed connection.

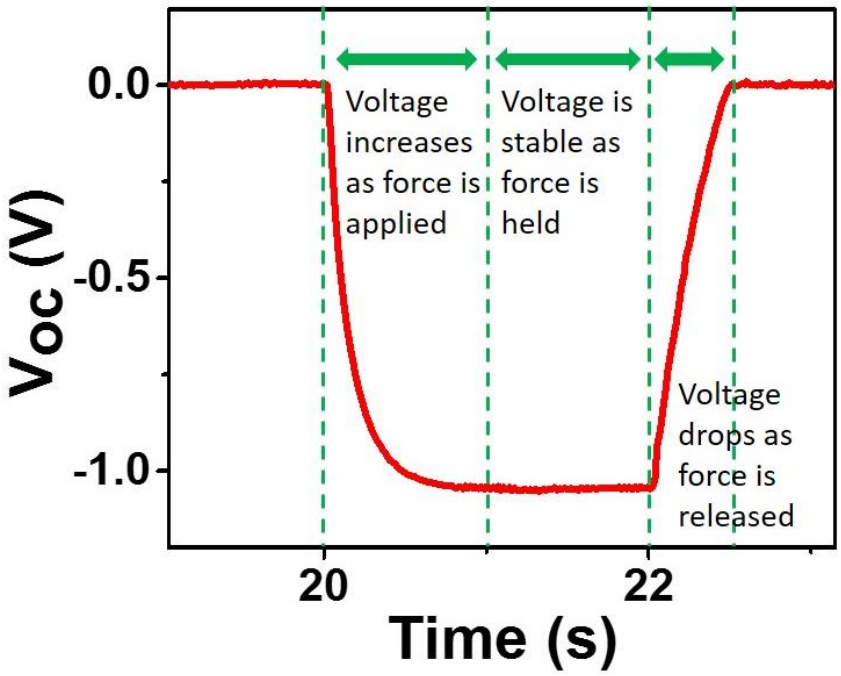

Figure A 5. Stability of the generated voltage over time. The constant voltage indicates extremely low leakage current, owing to the excellent dielectric property of FF microrods. The duration of the dwell in applied force in Figure 27c,d was doubled here to confirm the negligible decay of the open-circuit voltage output.

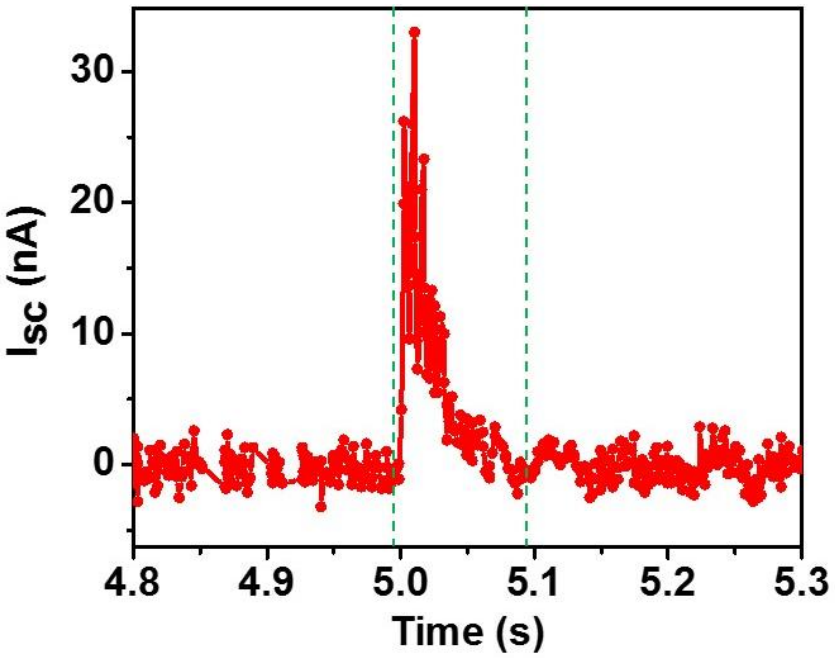

Figure A 6. Zoom-in view of a short-circuit current peak. The width of the current peak is about 100 ms. The current could be still generated after 100 ms but was not visible due to noise in the measurement system.

Table A 1. Summary of phase responses of microrods from the positive-EF growth, negative-EF growth, and no-EF growth.

Rod #	Phase response (degree)		
	Positive EF microrod	Negative EF microrod	No EF microrod
1	184	17.5	10
2	183	13.5	191.5
3	182	8.5	183
4	183.5	6.5	181.5
5	183.5	5.5	17
6	183.5	5.5	6.5
7	183	5.5	183.5
8	187.5	5.5	183.5
9	183.5	7.5	184.5
10	182.5	10.5	180.5
11	200.5	5	182
12	191.5	11	186
13	191.5	9.5	181.5
14	183	9.5	8
15	183.5	12	9.5
16	184	6	184
17	185.5	8.5	183
18	182.5	185.5	184
19	179	6.5	184
20	183.5	7	183.5

Table A 2. Summary of generated charges calculated by the integration of short-circuit current peaks over time.

Peak #	**Charge generated (pC)**	**Peak #**	**Charge generated (pC)**
1	509	6	551
2	522	7	539
3	477	8	521
4	598	9	506
5	504	10	568
Average	**530 pC**		